Numerical Investigation of Marine Propeller Underwater Radiated Noise Using Acoustic Analogy

Part 2: The influence of eddy viscosity turbulence models

Savas Sezen[1*], Taner Cosgun[2], Ahmet Yurtseven[2], Mehmet Atlar[1]

[1]University of Strathclyde, Glasgow, UK
[2]Yildiz Technical University, Istanbul, Turkey

Abstract

The present study focuses on the impact of eddy viscosity turbulence models on the benchmark INSEAN E779A marine propeller hydroacoustic performance under non-cavitating and open water conditions. In the numerical calculations, Realisable k-epsilon (k-ε), k-ω Shear Stress Transport (k-ω SST) and Spalart-Allmaras turbulence models, which are widely used in hydrodynamic fields, are selected. Hydroacoustic performance of the model propeller is predicted with the porous FW-H formulation and is coupled with the Reynolds-averaged Navier Stokes (RANS) solver. This study aims to show the effects of different turbulence models on marine propeller hydroacoustic performance at high and low blade loading conditions both in the near and far-fields. The numerical results show that the underwater radiated noise (URN) levels, which are predicted by using different eddy viscosity turbulence models together with the porous FW-H formulation, are found to be similar at low blade loading conditions. The reason behind this similarity is due to the analogous wake structure and hydrodynamic field. However, when the propeller loading is high, the propeller's wake loses its stability; hence, the coherent vortex structures break-up and evolve into the far-field of the propeller's slipstream. The instability process of the propeller's wake is predicted in a different manner by eddy viscosity turbulence models, and these differences cause dissimilar prediction of the URN in the far-field. Consequently, the underwater pressure field is considerably affected by the instability of the vortex structures (as a non-linear noise source) for far-field noise estimations. As a result, vortex instability in the propeller's slipstream might be the main noise source of the URN for far-field noise estimations under non-cavitating and high loading conditions.

Keywords: Underwater Noise, porous FW-H, Hydroacoustic, RANS, Turbulence Modelling.

1. Introduction

Investigation of the hydrodynamic noise has become of great interest in maritime studies due to the dramatic increase in anthropogenic noise sources in the oceans. Over the past years, the URN levels induced by the shipping activities have increased around 12dB (Hildebrand, 2009). Furthermore, as the ship traffic nearly doubled in the oceans between 1950-2000, the low-frequency ambient noise levels in the oceans increased approximately 10 dB or more between 1950-1975 (Ross, 1976). Due to this fact, rising concern about the harmful effects of noise pollution caused by the shipping activities has forced governments and international societies to study for possible solutions to mitigate its impact on the marine ecosystem. Therefore, international non-mandatory rules such as DNV-GL QUIET class and RINA DOLPHIN notations are becoming more widespread to minimise the noise pollution in the oceans. Additionally, the primary threat of underwater noise pollution was also recognised by the International Maritime Organization (IMO) for the reduction of URN levels, mainly radiated by commercial shipping (IMO, 2014).

The main noise sources for the ships can be classified into three sections as machinery noise, hydrodynamic flow noise, and propeller URN (ITTC, 2014a). Amongst the different types of noise sources, URN induced by marine propellers has a crucial role both under non-cavitating and cavitating conditions. For this reason, the cavitating propeller noise can be considered as more critical than the non-cavitating propeller URN, especially for commercial and passenger ships due to its negative influence on marine fauna, passenger comfort, etc. As is well known, in the presence of the cavitation, underwater pressure fluctuations increase rapidly due to the unsteady behaviour of the cavitation and explosion of the vapour bubbles. It consequently results in higher noise levels. On the other hand, non-cavitating propeller URN mainly occurs due to the fluctuation of the hydrodynamic forces on the propeller blade, and it is classified into two parts, namely discrete frequency (tonal) and continuous spectrum (broadband) (ITTC, 2014a). The prediction of non-cavitating propeller URN is also critical for the naval vessels and submarines to prevent acoustic detection, particularly by sonars. When propeller URN is reduced, it enables a significant decrease in the overall noise levels of the ships. For this reason, mitigation of the propeller URN is an important design task for marine propellers. In order to achieve low noise levels, propeller URN should be kept as minimum as possible, particularly in design stages (Ebrahimi et al., 2019).

Over the years, propeller hydrodynamic performance and URN have been predicted by using experimental and numerical techniques (i.e. potential or viscous based solvers). Moreover, semi-empirical calculations are still implemented to predict the propeller URN in the preliminary design stage. Having said that numerical methods have become more attractive for the prediction of the propeller URN in recent years. The reason behind this, acoustic analogies which are generally used in aeroacoustics community are now employed in the hydroacoustic field.

Without a doubt, the solution of the hydrodynamic field around the propeller has several challenges. These challenges, especially for RANS based-solvers calculations, can be mainly considered as the accurate resolution of the boundary layer, accurate assessment of the vortex structure in the propeller's slipstream, computation of unsteady behaviour of the flow features, etc. (Spalart, 1999; Dacles-Mariani et al., 1999). Additionally, numerical prediction of the hydroacoustic pressures needs an appropriate resolution of the flow field to capture the low-amplitude acoustic signal because of the possible numerical errors and dissipation, which are generally introduced by numerical solvers. Hence, these numerical errors might cause a crucial part of the noise signal to be eliminated (Sengupta et al., 2006). The level of numerical dissipation in the RANS based calculations is mainly originated from both discretisation errors (grid or mesh structure) and insufficient turbulence modelling (Feder and Abdel-Maksoud, 2016). Therefore, selection of the proper grid resolution and turbulence model has paramount importance for the hydrodynamic and hydroacoustic calculations.

The effects of the grid structure and turbulence modelling on propeller hydrodynamic performance were studied in several studies in the literature. In the study of Morgut and Nobile (2012), the flow around the marine propellers (i.e. the five-bladed propeller P5168 and INSEAN E779A) was solved under non-cavitating and uniform flow conditions. The effects of hexa-structured and hybrid unstructured meshes, SST and BSL-RSM (Baseline-Reynolds Stress Model) turbulence models on propeller global performance characteristics (i.e. thrust and torque coefficients), were investigated. The numerical results were found to be similar for both hexa-structured and hybrid-unstructured types of grids. Moreover, it was found that BSL-RS M turbulence model provides slightly better predictions in comparison to two equations SST turbulence model in terms of the propeller open water characteristics. Wang

and Walters (2012) solved the flow around the model propeller (i.e. P5168) by using a three-equation transition-sensitive k-ω and standard k-ω SST models. The main objective of the study was to compare the flow characteristics obtained by two different turbulence models. The numerical results showed that the sensitive k-ω turbulence model captures blade-surface stresses, flow separations and the flow properties in the vortex cores more accurately. In contrast, the standard k-ω SST model induces an excessive amount of dissipation in the vortex cores. Besides, the thrust and torque coefficients were predicted with good accuracy by using a transition-sensitive turbulence model, especially at high loading conditions. Ji et al. (2012) solved the cavitating flow around the marine propeller by using a modified k-ε turbulence model, which was named as Partially-Averaged Navier–Stokes (PANS) model. The proposed turbulence model is based on the k-ε turbulence model. The results indicated that the modified turbulence model solves the flow field better than the k-ε turbulence model in the propeller's slipstream. Peng et al. (2013) examined the effects of turbulence models on the tip vortex flow for a marine propeller under non-cavitating conditions. The numerical results indicated that eddy viscosity turbulence models predict the tip vortex flow and global performance characteristics slightly better than Reynold Stress Turbulence Models (RSM). In addition, it was found that the circumferentially averaged velocities, which are outside of the tip vortex region, are not significantly affected by the different solutions of turbulence models. Muscari et al. (2013) solved the flow around the non-cavitating marine propeller by using DES (Detached Eddy Simulation) and RANS solvers with the Spalart-Allmaras turbulence model. The main aim of the study was to investigate the hydrodynamic characteristics of the propeller and wake instability in the propeller's slipstream at two loading conditions. In the numerical calculations, RANS simulations were conducted in a steady manner, whereas unsteady DES simulations were performed. As a result of the study, RANS solver predicted thrust and torque values better than DES solver. However, vortex instability in the propeller's wake was predicted with good accuracy in DES solver. Guilmineau et al. (2015) examined propeller hydrodynamic performance and propeller's wake instability for a wide range of advance coefficients under non-cavitating condition. In the numerical calculation, the k-ω SST and EARSM (Explicit Algebraic Reynolds Stress Model) and DES with k-ω SST were employed. The numerical results were compared with the experiment in terms of the vorticity distribution and global performance characteristics. While thrust and torque values were found to be in a good agreement with the experiment for different models, dissipation of the

flow properties in the propeller's wake was found to be higher in steady k-ω SST and EARSM RANS models. Hence, the propeller's wake instabilities could not be adequately predicted in RANS based calculations in comparison to the DES approach. Baek et al. (2015) investigated the effects of the advance ratio on the evolution of a propeller's wake instabilities using an unsteady RANS approach for KP505 model propeller in open water conditions. Numerical simulations were performed for a wide range of advance ratios from J=0.2 to J=0.6. Based on the numerical results, empirical models for the 3-D helices of tip vortices were proposed. It was stated that the propeller's wake could be reliably modelled by using empirical models. In a recent study of Sikirica et al. (2019), hydrodynamic performance of the benchmark PPTC (Potsdam Propeller Test Case) model propeller was investigated both under non-cavitating and cavitating conditions. The RANS based models and two different commercial tools (i.e. Star CCM+ and Ansys Fluent) were used for a wide range of advance ratios. The accuracy of the Realisable k-ε and k-ω SST turbulence models were investigated by using structured and unstructured grids. The numerical results indicated that two different grid structures provide similar results in a specific range of advance ratios. However, the structured grid with the Realisable k-ε model yields more accurate results, especially at low and high advance ratios in terms of propeller global performance characteristics.

To summarise, different viscous solvers (i.e. RANS, DES or LES (Large Eddy Simulation)) and turbulence models have been used for the solution of the flow field around the marine propellers over the years. In these studies, propeller hydrodynamic characteristics, unsteady flow features, and particularly instability processes of the propeller's wake, were mainly investigated. In recent years, with an increasing interest in the propeller URN studies, CFD (Computational Fluid Dynamics) tools (i.e. potential and viscous solvers) have also been started to use together with the acoustic analogies as a hybrid method (i.e. viscous or potential based hydrodynamic solvers + acoustic analogy). In this way, the acoustic analogy is employed to propagate the information from near field to far-field (i.e. selected receiver locations) as a transfer function. The most commonly used acoustic analogy both in aeroacoustics and hydroacoustic fields is the Ffowcs-Williams Hawkings (FW-H) formulation (Ffowcs Williams and Hawkings, 1969).

In the past, potential based BEM (Boundary Element Method) solvers together with Farassat 1A (Farassat, 2007) formulation, which is the proposed solution of the FW-H equation, was first implemented to investigate the effects of the duct on propeller URN in non-uniform flow conditions (Seol et al., 2002). Later, the authors extended their investigation for the prediction of propeller URN in the presence of the sheet cavitation (Seol et al., 2005). The modified version of Farassat 1A (Farassat, 2007) formulation was also implemented together with BEM solver for the investigation of bubble evolution with time in the presence of sheet cavitation (Ianniello, 2015). Apart from the potential solvers, viscous solvers have become popular for the investigation of propeller URN together with acoustic analogies under non-cavitating and cavitation conditions. Due to the increasing attention to viscous solvers, hydroacoustic analysis of the ship propellers including hull, rudder, and appendages have been generally started to conduct by using RANS with different resolution forms of the FW-H equation (i.e. impermeable and permeable/porous formulation). In the study of Ianniello et al. (2013), the RANS solver with the Spalart-Allmaras turbulence model was used to predict the benchmark INSEAN E779A model propeller URN under non-cavitating conditions by using different resolution forms of FW-H equation. The main aim of the study was to show the contribution of the non-linear noise term to the total hydroacoustic. The results showed that the contribution of non-linear noise terms which are mainly represented by turbulence and vorticity become to be dominant, especially far away from the propeller. The reason behind this was the rapid decay of the linear FW-H noise terms (i.e. thickness and loading) as far away from the noise source. Therefore, it was proved that marine propeller URN would not be able to evaluate accurately without taking the contribution of non-linear noise terms into account. Following the study of Ianniello et al. (2013), porous formulation of the FW-H equation was commonly performed together with the RANS solver to include the contribution of non-linear noise terms to overall propeller URN. In this regard, Lloyd et al. (2014; 2015a; 2015b) conducted research studies for the prediction of propeller URN by using a porous formulation of the FW-H equation together with k-ω SST turbulence model (i.e. RANS) for different receiver locations under non-cavitating conditions in the near field. Moreover, the application of scale resolving simulations (i.e. DES or LES) together with the FW-H equation is increasing for the prediction of marine propeller URN under non-cavitating conditions (Ianniello and De Bernardis, 2015; Testa et al., 2018; Cianferra et al., 2019).

The application of the hybrid methods is a relatively new research field for the prediction of the propeller URN. So far, the capabilities of the porous FW-H acoustic analogy have been mostly tested together with the RANS solver under non-cavitating and relatively lower blade loading conditions (i.e. higher advance ratios) in the near field. Undoubtedly, scale resolving simulations (i.e. DES or LES) increase the fidelity of the solution and capture more details of the flow field. However, all these favourable gains lead to a remarkable increase in computational cost. Due to this fact, RANS solvers become more attractive, especially for practical applications. Even though RANS solvers suffer from the numerical errors which mainly occur due to the insufficient grid resolution and turbulence modelling, it has been still used with the FW-H acoustic analogy, particularly for tonal noise predictions in the preliminary design stage. Furthermore, the effects of crucial solution parameters such as time step, grid structure, and dimensions of the porous surface on propeller hydroacoustic performance have still been investigated by using RANS based hybrid method. (Lidtke et al., 2019).

Within this framework, this study addresses the effects of different turbulence models on propeller URN both in near and far-fields under non-cavitating and two different loading conditions (i.e. low and high blade loading). For this reason, three different eddy viscosity turbulence models (i.e. Realisable k-ε, k-ω SST and Spalart-Allmaras) were selected. As given in the introduction part, several studies exist for the investigation of different eddy viscosity turbulence models on propeller hydrodynamic performance and unsteady flow features (e.g. propeller's wake instability). However, to the best of the authors' knowledge, there exists no specific numerical study to investigate its effects on propeller URN. Additionally, the influences of wake instabilities and the break-up of the tip vortices (as non-linear noise sources) on propeller URN have not been investigated yet. Thus, this study aims to fill these research gaps by using different turbulence models together with the porous FW-H formulation.

This paper is organised as follows: The background of the turbulence models is explained in Section 2. Section 3 presents the governing equations for both hydrodynamic and hydroacoustic parts. The test case and numerical details are given in Section 4. The hydrodynamic and hydroacoustic results are presented in Section 5 and 6, respectively. Finally, the conclusion part is presented in Section 7.

2. Background of Turbulence Modelling

Turbulent flow can be employed in the Navier Stokes equations to conduct the solutions of the chaotic flow behaviour. Furthermore, all dependent variables in the turbulent flow such as velocity, pressure, temperature, etc. change rapidly both in time and space due to the random nature of the turbulence. However, the numerical prediction of the rapid variations in instantaneous flow characteristics is a difficult task. DNS (Direct Numerical Simulation) is the way to solve the Navier-Stokes equations with instantaneous values. Yet, DNS computations require significant effort and computational power as the scales of turbulent structures vary in a broad range; thus, resolution of the flow around the complex geometries and high Reynolds number flows are not possible using DNS. For this reason, using statistically averaged variables become a more practical and useful way for the calculation of turbulent flow in order to prevent the computational cost of the DNS method.

The instantaneous values can be considered as the sum of their mean and fluctuating parts (i.e. $u_i = \bar{u} + u'$ here, $\bar{u}$ is the mean value and u' is the fluctuation part) in the turbulent flow. This discretisation is known as Reynolds decomposition (Versteeg and Malalasekera, 2007). By substituting of decomposed variables into the N-S equation and applying an averaging procedure, governing equations (i.e. RANSE, Reynolds-averaged Navier Stokes Equations) can be obtained for turbulent flow. In RANS equations, time-averaged flow properties are similar to those of N-S equations, except Reynolds Stress term $(\overline{u'_i u'_j})$. However, due to lack of required equations for the solution of the new terms, unknown variables occur; thus, this problem is called a **closure problem** (Pope, 2000). Several approaches have been implemented for modelling of the Reynolds stresses for years. The first proposed models are Prandtl's mixing length (Prandtl, 1949) and Boussinesq's eddy-viscosity concepts (Wilcox, 2006). Since these models do not have additional partial differential equations, they are generally known as algebraic and zero equation turbulence models. In addition to the fact that they were successfully used for simple flow problems in the past. However, new turbulence models were required due to their inadequacy for the more complex flow problems. The majority of the turbulence models are based on the solution of the additional transport equations such as Reynolds stresses, turbulent kinetic energy, and dissipation. Therefore, they are commonly used to solve more complex flow problems in comparison to algebraic models (Cebeci, 2013). In this regard, k-ε and k-ω (two-equation) and Spalart-

Allmaras (one-equation) models and their variants are commonly used to close the governing equations in the hydrodynamic field.

2.1 k-ε turbulence model and its variants

k-ε turbulence model might be considered as the most popular turbulence model in engineering calculations, probably for being the first applied one in practice. It mainly focuses on the processes that cause a change in the turbulent kinetic energy (Versteeg and Malalasekera, 2007). In this model, two transport equations (i.e. turbulence kinetic energy and dissipation rate) are computed to represent the effects of turbulent stresses on eddy viscosity. The earlier proposed coefficients were revised with those suggested by Launder and Sharma (1974), and it was started to be referred to Standard k-ε turbulence model. (Wilcox, 2006). Following that, the application of the Standard k-ε turbulence model became popular, and it was integrated with many commercial CFD codes (Pope, 2000). It is to be noted that the k-e turbulence model and its variants are available in Star, CCM+ (Star CCM+, 2019). The Standard k-ε turbulence model uses the wall functions to model the universal behaviour of the near-wall flows at high Reynolds numbers. In contrast, the drawback of the Standard k-ε turbulence model is that it is not suitable for the low Reynolds number type flows since the log-law is not valid near solid boundaries. Therefore, several modified versions of the Standard k-ε model were proposed for both low and high Reynolds number type flows (Versteeg and Malalasekera, 2007).

One of the modified versions of the standard model is the Realisable k-ε model that has been extensively used for practical ship hydrodynamic problems (Shih et al., 1995). In this model, a new transport equation was proposed for the turbulent dissipation rate. Besides, a new formulation was introduced for the calculation of turbulent viscosity coefficient, which is constant in Standard k-ε. Thus, it became a non-linear version of the Standard k-ε model, and additional effects were included to account for Reynolds stress anisotropy (Sadrehaghighi, 2019). As a result, Realisable k-ε model provides better predictions in many applications, particularly for separating flows and some unconfined flows compared with the Standard k-ε model (Bulat and Bulat, 2013; Tu et al., 2018).

Another variant of the Standard k-ε model is the Abe-Kondoh-Nagano (AKN) k-ε model, which was proposed to model the low-Reynolds number type flows (Abe et al., 1994). AKN k-ε model has different coefficients and damping functions in comparison to other models. It is considered that the AKN k-ε model predicts average flow and turbulent quantities in

separating flows better than the standard model. Additionally, another widely used turbulence model is the v^2f k-ε turbulence model (Durbin, 1991). It is the improved version of Standard k-ε model, and it combines the anisotropy of the near-wall turbulence and non-local pressure-strain effects (Sundén and Fu, 2017). In addition to the solution of the kinetic and dissipation rate equations, the v^2f k-ε model also solves two more transport equations, which are wall-normal stress component 'v^2' and elliptic relaxation parameter 'f'. Besides, it solves the near-wall flow without the need of using wall-function. Some modifications were applied for the source terms and non-isotropic turbulence viscosity to improve the capabilities of the model (Davidson et al., 2003). It is claimed that v^2f k-ε turbulence model is more accurate than traditional two-equation eddy viscosity models for the solution of flow separation, wall friction, and representation of the near-wall turbulence effects (StarCCM+,2019; Luo and Razinsky, 2008).

2.2   k-ω turbulence model and its variants

The second widely used two-equation transport model is the k-ω model and its variants. Similar to k-ε models, the Standard k-ω model solves a transport equation for turbulence kinetic energy 'k' for determination of turbulent eddy viscosity (Wilcox, 2006). However, the dissipation rate (ε) is replaced with turbulence frequency (ω), which is the dissipation rate per unit turbulent kinetic energy. According to Sadrehaghighi (2019), the main difference between k-ε and k-ω turbulence models are dissimilar trends of ε and ω at the solid walls and different description of the wall boundary conditions for the same variables. It is believed that the superiority of the k-ω model is to show better performance for the solution of the boundary layer under adverse pressure gradients (i.e. separated or swirled flows) (StarCCM+, 2019). Nevertheless, the k-ω turbulence model is sensitive to the free stream value of ω; hence, it needs to be described carefully (Tu et al., 2018).

The k-ω SST (Shear Stress Transport) model was derived by Menter (1994) as the modified version of the Wilcox's k-ω model. In this model, the robust & accurate formulation of the Standard k-ω model in the near solid surfaces and benefits of the free stream independence of the k-ε model in the outer region were combined (Poncet et al., 2010). The k-ω SST model is available in many commercial CFD tools, and the popularity of the model increases for the solution of the hydrodynamic problems because of the several advantages in comparison to other models. For this reason, it was selected to investigate its capabilities in terms of

prediction of propeller's wake instability and propeller URN at two different loading conditions in this study.

2.3   One equation turbulence models

One equation turbulence closure models were proposed as an alternative to the two equations turbulence models for the calculation of the eddy viscosity. The most popular one-equation model is the Spalart-Allmaras model (Spalart and Allmaras, 1992). This closure uses a transport equation for the calculation of eddy viscosity. The Spalart-Allmaras model is more computationally more affordable than other two-equation models since it solves only one additional equation. While the Spalart-Allmaras model is a suitable model for the for free-shear and boundary-layer flows, it is claimed that it may have disadvantages for the computations of shear flow, separated flow, or decay of turbulence (Zhai et al., 2007; Sadrehaghighi, 2019). It should be noted that this model was initially developed for aerodynamic applications. As there are several studies in the literature, especially in the propeller hydrodynamic and hydroacoustic fields, its capabilities were investigated in terms of the propeller URN in the present study.

The summary of the implemented turbulence models is also presented in Table 1. Detailed mathematical descriptions and references about the models which were implemented can be found in commercial solver documentation (StarCCM+, 2019).

Table 1. Selected turbulence models.

One equation turbulence model	Spalart-Allmaras
Two Equations turbulence models	k-ω SST
	Realisable k-ε

3. Numerical Model

In this section, fundamental equations of the CFD method based on the Navier-Stokes equations are briefly explained. Following the hydrodynamic section, the hydroacoustic model is introduced.

3.1   Numerical Model

The hydrodynamic model uses the continuity and momentum equations in an incompressible form. The incompressible form of the continuity equation is given as follows.

$$\frac{\partial u_i}{\partial x_i} = 0$$
(1)

The incompressible form of the momentum equation is;

$$\frac{\partial u_i}{\partial t} + u_j \frac{\partial u_i}{\partial x_j} = -\frac{1}{\rho}\frac{\partial P}{\partial x_i} + \vartheta \nabla^2 u_i + F_i \tag{2}$$

Here, u is the velocity, m/s; ρ is the density, kg/m3; ϑ is the kinematic viscosity, m2/s; $\nabla^2 u_i$ is the viscous term, P is the pressure; Pa, F_i is the body forces; N.

3.2   Hydroacoustic Model (FW-H Equation)

Prediction of URN induced by the marine propeller is becoming widespread by using hybrid methods (i.e. incompressible hydrodynamic solver + acoustic analogy). The application of the acoustic analogies provides the prediction of the radiated noise by using the hydrodynamic results. In this way, the source and propagation fields can be decoupled. First, the source field is determined using incompressible solvers, and then acoustic analogies are used for the propagation of sound from near field to far-field as a transfer function. The most commonly implemented method is Ffowcs-Williams Hawkings (FW-H) equation (Nitzkorski, 2015), which has been commonly used both in aeroacoustics and hydroacoustic fields.

FW-H equation is the rearrangement form of the continuity and momentum equations into the wave equations. In this equation, noise sources are represented by monopole, dipole and quadrupole terms (Ffowcs Williams and Hawkings, 1969). The contribution of the monopole and dipole noise terms (i.e. linear terms) is evaluated by solving the surface integrals on the noise source. However, the quadrupole noise term needs volume integral solutions. The generalised function of the FW-H equation can be expressed as,

$$\left(\frac{1}{c_0{}^2}\frac{\partial^2}{\partial t^2} - \nabla^2\right)p(x,t) = \frac{\partial}{\partial t}\{[\rho_0 v_n + \rho(u_n - v_n)]\delta(f)\} -$$

$$\frac{\partial}{\partial x_i}\{[\Delta P_{ij}n_j + \rho u_i(u_n - v_n)]\delta(f)\} + \frac{\partial}{\partial x_i \partial x_j}\{T_{ij}H(f)\} \tag{3}$$

First-term on the right side of the Equation 3 is the monopole (i.e. thickness) noise term, the second one is dipole (i.e. loading) noise term, and the latter one is the quadrupole (i.e. non-linear) noise term. Here, p identifies the total acoustic pressure, Pa; T_{ij} ($T_{ij} = \rho u_i u_j + P_{ij} - c_0{}^2\tilde{\rho}\delta_{ij}$) is Lighthill stress tensor, N; u_i and v_i are the fluid and surface velocity components, m/s, respectively. $\tilde{\rho}$ ($\tilde{\rho} = \rho - \rho_0$) is the density perturbation, kg/m^3 to the undisturbed medium and n indicates the projection along the outward normal to the surface. Additionally, c_0 is the sound speed, m/s; P_{ij} represents the compressive stress tensor, N ($\Delta P_{ij} = P_{ij} - p_0\delta_{ij}$). Here, δ_{ij} is the Kronecker operator.

In the aeroacoustics field, the quadrupole noise term becomes important, especially at high supersonic and transonic regimes. Thus, the acoustic field is generally dominated by linear noise terms (i.e. monopole and dipole) in most aeronautical problems. Due to this reason, FW-H equation is evaluated by only taking two linear terms into account. This form of the FW-H equation is also known as Farassat 1A (Farassat, 2007). On the other hand, any reliable hydroacoustic results need to include volume integral solution due to the rapid decay of the linear terms in the far fields (Ianniello et al., 2013). Hence, the porous resolution form of the FW-H equation, which was first implemented by Ffowcs Williams and Hawkings (1969) and proposed as a possible solution of the FW-H equation by Di Francescantonio (1997) becomes appealing. Porous form of FW-H equation enables to compute the non-linear noise term without any need for volume integration, which decreases the computational cost of the solution. In porous FW-H approach, which is implemented in this study, two new variables are introduced as modified velocity and modified stress tensor as given in Equation 4 and 5.

$$U_i = u_i + (\frac{\rho}{\rho_0} - 1)(u_i - v_i) \tag{4}$$

$$L_i = P_{ij}n_j + \rho u_i (u_n - v_n) \tag{5}$$

The permeable or porous region surrounds the propeller and relevant part of the propeller's slipstream where non-linear effects are important. In porous FW-H formulation, the monopole and dipole noise terms of Farassat 1A (Farassat, 2007) lose their original physical meanings. Thus, they become 'pseudo monopole' and 'pseudo-dipole' terms which include the contribution of the quadrupole term. Porous FW-H formulation can be written as follows for a stationary porous domain under the incompressibility assumption (Di Francescantonio, 1997).

$$4\pi p(x,t) = \int_S \frac{\rho_0 \dot{U}_n}{r} dS + \int_S \frac{\dot{L}_r}{c_0 r} dS + \int_S \frac{L_r}{r^2} dS + p_Q(x,t) \tag{6}$$

Where, r (m) is the distance between the noise source and the receiver, subscripts r and n define the dot product of a quantity with a unit vector either radiation or normal directions, respectively. The last term of Equation 6 represents the non-linear contribution of the noise sources outside of the porous surface in the fluid domain. It was considered that the extension of the porous surface nearly encompasses all relevant non-linear noise sources; thus the non-

linear contribution outside of the porous domain was neglected in this study similar to other studies in the literature (Ianniello et al., 2013; Ianniello and De Bernardis, 2015).

4. Test Case and Numerical Strategy

4.1 Propeller Geometry

The benchmark INSEAN E779A model propeller was selected because of the available experimental hydrodynamic data (see, e.g. Calcagno et al., 2006; Salvatore et al., 2009 and Felli et al., 2011). Table 2 summarises the main particulars of the model propeller, whereas Figure 1 shows the 3-D view of the propeller.

Table 2. Main particulars of the propeller.

Number of Blades	4
Diameter (m)	0.227
Pitch Ratio (P/D)	1.1
Expanded Area Ratio (A_E/A_0)	0.69
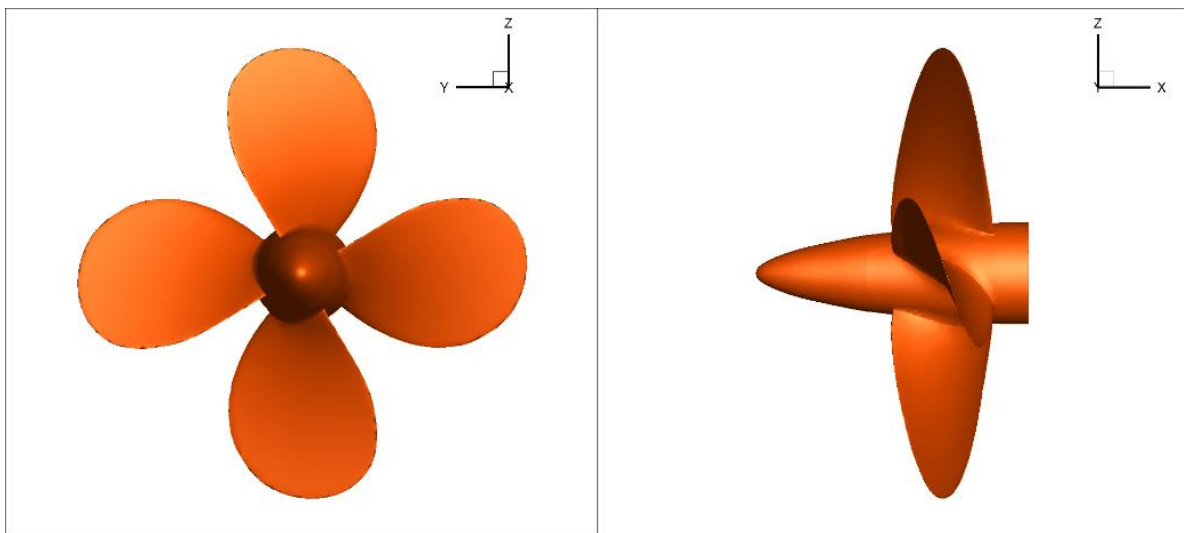
Figure 1. Back and side views of the INSEAN E779A model propeller.

In the numerical calculations, the propeller rotational speed was kept constant at 25rps. The inflow velocities were set to V_A=5 and 1.7m/s corresponding to J=0.88 and J=0.3, respectively. The advance coefficient (J), non-dimensional thrust (K_T), torque coefficients ($10K_Q$), and open water efficiency (η_0) can be calculated as follows.

$$J = \frac{V_A}{nD} \tag{7}$$

$$K_T = \frac{T}{\rho n^2 D^4} \tag{8}$$

$$K_Q = \frac{Q}{\rho n^2 D^5} \tag{9}$$

$$\eta_0 = \frac{J}{2\pi} \frac{K_T}{K_Q} \tag{10}$$

where, V_A is the inflow velocity; m/s, n is the propeller rotational speed; 1/s, D is the propeller diameter; m, T is the thrust; N, Q is the torque; N.m and ρ is the density of water; kg/m^3.

4.2   Numerical Strategy

The hydrodynamic and hydroacoustic simulations were carried out by using commercial CFD software (StarCCM+, 2019). In the numerical calculations, the governing equations are discretised based on the finite volume method. Temporal and spatial discretisation was done by using a second-order scheme to increase the accuracy of the solution. Besides, implicit unsteady schemes were applied for all simulations. Segregated flow solver with SIMPLE type solution algorithm was imposed on the calculations. Three different turbulence models were used to close the Navier-Stokes equations as given in Table 1 with the same grid structures. In the numerical calculations, y+ values on the propeller blades were calculated between 30 and 40 by using all y+ treatment method in Star CCM+ at two different loading conditions (StarCCM+, 2019). The propeller rotational motion was modelled by using RBM technique (Rigid Body Motion method or so-called sliding interface).

The numerical simulations were started in a steady manner until the flow properties converged in the computational domain. The reason for this, the steady solution served as an initial step to unsteady calculations to speed up the convergence process. After that, the unsteady simulations were run around 40 propeller revolutions. During the simulations, the convergence of the hydrodynamic variables (i.e. pressure, velocity, etc.) was checked before moving to the propeller URN. Later, acoustic pressures were collected at different receiver locations by using FW-H acoustic analogy.

4.3   Computational Domain & Boundary Condition Design

The cylindrical computational domain was used in the numerical calculations. The radial dimension of the domain was set to 8D. In our experience, the downstream extension of the domain from the propeller centre is crucial to prevent the spurious noise created by outlet boundary. Thus, the axial extension of the domain was set 10D to allow the evolution of the flow in the propeller's slipstream (i.e. upstream: 3D and downstream: 7D from the propeller blade centre) and reduce the spurious noise as much as possible. Besides, the transition

between rotating and static regions was provided by a rotating interface (sliding interface). Figure 2 shows the computational domain and boundary conditions.
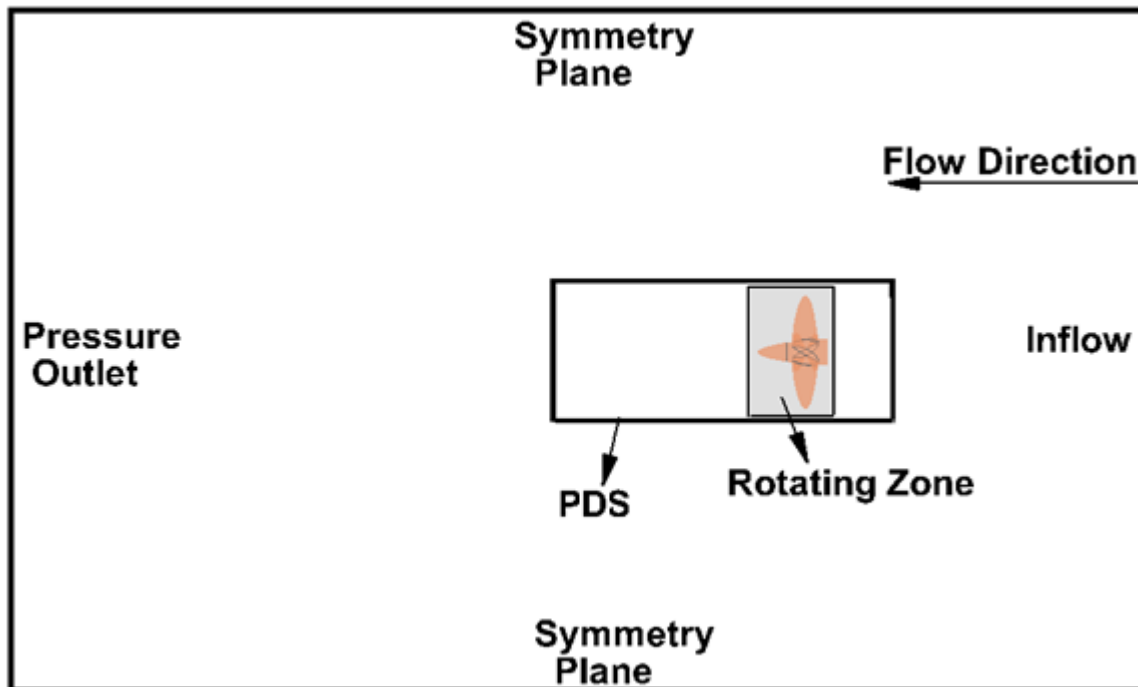

Figure 2. Representation of the computational domain (Figure is not scaled).

In the numerical calculations, porous or permeable data surface (PDS) was placed outside of the interface region (i.e. between two grid domains) to encompass the relevant non-linear noise contributions as much as possible. The PDS consists of a main cylinder and two end caps. It should be noted that porous acoustic analogies require the end-cap scheme to suppress the spurious noise due to the truncation errors. Therefore, an open-ended PDS, which is strongly proposed in the study of Ianniello and De Bernardis (2015), was used to collect the acoustic pressures both in near and far-fields (Nitzkorski, 2015). The exact locations and dimensions of the PDS have still been discussed in the literature (Li et al., 2018; Lidtke et al., 2019).

4.4 Grid Structure

The unstructured grid with hexahedral elements was employed to discretise the computational domain. Hydroacoustic simulations are considered to be more sensitive to mesh quality and density than propeller hydrodynamic simulations. For this reason, the grid resolution needs to be determined carefully to resolve/model the sound-induced by turbulent scales. It should also be able to resolve the acoustic waves properly towards the far-field hydrophone locations (Star CCM+, 2019). One of the important noise sources can be

considered as numerical noise induced by sliding interfaces (i.e. mesh transitions) in rigid type meshes. Hence, the selection of grid structure is important to prevent the deterioration of the overall acoustic pressures in the numerical calculations. The impact of the grid structure on propeller hydroacoustic performance was also discussed in the 27th ITTC discussion form (ITTC, 2014b) and recommendations were given. It is to be noted that a comprehensive study on the effects of grid structure on propeller URN was performed in our Part 1 study (Sezen et al., 2020). In the simulations, a suitable region-based grid structure was adopted by using trimmer mesh approach (Figure 3). Uniform grid resolution with the cells, which have minimal skewness and high quality were employed in the computational domain. In order to prevent the numerical noise induced by sliding interfaces (i.e. mesh transitions), the cell sizes were kept constant inside the PDS (StarCCM+, 2019).
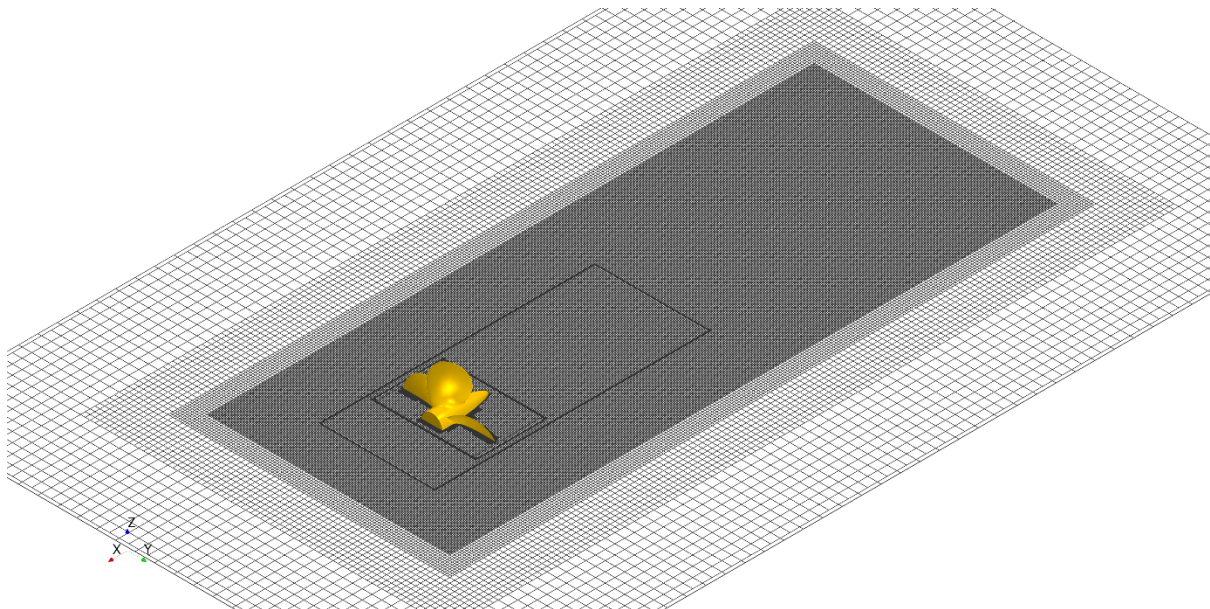
Figure 3. Grid structure around the propeller blades (Finest Grid)

4.5 Uncertainty assessment of the numerical study

Uncertainty study was conducted by using the methodology proposed by Roache (1997) for propeller global performance characteristics (i.e. non-dimensional thrust and torque). The reason behind this, to the best of author's knowledge, there is no specific uncertainty method for the evaluation of propeller URN simulations in the literature. In the proposed methodology, three different solutions are desired to be an accurate assessment of the numerical solution. However, according to Roache (1997), two solutions can also be used to calculate the uncertainty level of the solution. Therefore, the uncertainty of the numerical solution was evaluated by using two different grid resolutions, which has 18.5 M and 7M total

element count. The solution scalars were selected both thrust and torque coefficients at J=0.88. Furthermore, the k-ω SST turbulence model was utilised for the uncertainty study. The solution variation can be estimated in the proposed uncertainty methodology as follows.

$$E = \frac{f_2 - f_1}{1 - r^p} \tag{11}$$

Here, f_1 and f_2 represent fine and coarse grid solutions, respectively. r is the refinement factor, and p is the formal order of accuracy. In the numerical calculations, r was selected $\sqrt{2}$, whereas p was selected 2. Then, the uncertainty of the numerical solution can be calculated with the following equation.

$$U_N = F_s|E| \tag{12}$$

where F_s is a safety factor and it was taken as $F_s = 3$, according to Roache (1997).

Non-dimensional K_T and $10K_Q$ values and the uncertainty value of the solution can be seen in Table 3. As a result of the uncertainty study, fine grid structure was employed for all turbulence models at two different loading conditions.

Table 3. Uncertainty of the numerical solution.

Grid	Coarse	Fine	U_N (%)
K_T	0.152	0.149	0.9
$10K_Q$	0.310	0.306	1.2

5. Hydrodynamic Results

In this section, the numerical hydrodynamic results of the benchmark propeller are presented at two different loading conditions.

5.1 Propeller Global Performance Characteristics

Table 4 shows the comparison of non-dimensional thrust and torque values with the experimental data for different turbulence models at two different loading conditions. As can be seen in Table 4, propeller performance characteristics were predicted with good accuracy by using different turbulence models. It can be concluded that there is no significant difference between turbulence models for the prediction of thrust and torque values.

Table 4. Comparison of propeller hydrodynamic characteristics at two different loading conditions.

Quantity	J=0.88			J=0.3		
	Spalart-Allmaras	k-ω SST	Realisable k-ε	Spalart-Allmaras	k-ω SST	Realisable k-ε
K_T (CFD)	0.152	0.149	0.150	0.424	0.425	0.426
K_T (EFD)	0.151			0.430		
ΔK_T (%)	0.662	1.325	0.662	1.395	1.162	0.930

$10K_Q$ (CFD)	0.309	0.306	0.308	0.712	0.721	0.723
$10K_Q$ (EFD)	0.305			0.707		
$\Delta10K_Q$ (%)	1.311	0.328	0.983	0.707	1.980	2.263

5.2 Investigation of Flow Field in the Propeller`s Slipstream

The flow field analysis in the propeller`s slipstream is performed at two different advance coefficients (i.e. J=0.8 and J=0.3), and the numerical results are compared with the available experimental data.

5.2.1 J=0.88

The flow around the marine propeller is a complex phenomenon both in the presence of the hull and isolated condition (i.e. open water or uniform flow). Therefore, a detailed investigation of the flow field in the propeller's slipstream is of great importance as it is directly related to noise, vibration, and propulsion performance of the marine propellers. The propeller's wake consists of two systems of vortex structures, which are mainly generated at the blade's root and tip sections. The tip vortices originate from the pressure difference between face and back sides of the blades. A sheet of trailing vortices because of the non-constant circulation and axial hub vortex can be considered as additional vortex structures. Beside, vortex/vortex interactions may cause the vortex instabilities, and it is still under investigation by using experimental and numerical techniques (Felli et al., 2011; Muscari et al., 2013; Kumar and Mahesh, 2017).

The vorticity distribution in the Y direction is given in Figure 4 for three different turbulence models with the experimental visualisation at J=0.88 (Salvatore et al., 2006). The extension of tip vortices in the propeller's slipstream was found to be in a good agreement with the experimental measurement by using different turbulence models. Nevertheless, the accuracy of the RANS solutions to predict the flow details inside the vortex core might be questionable.
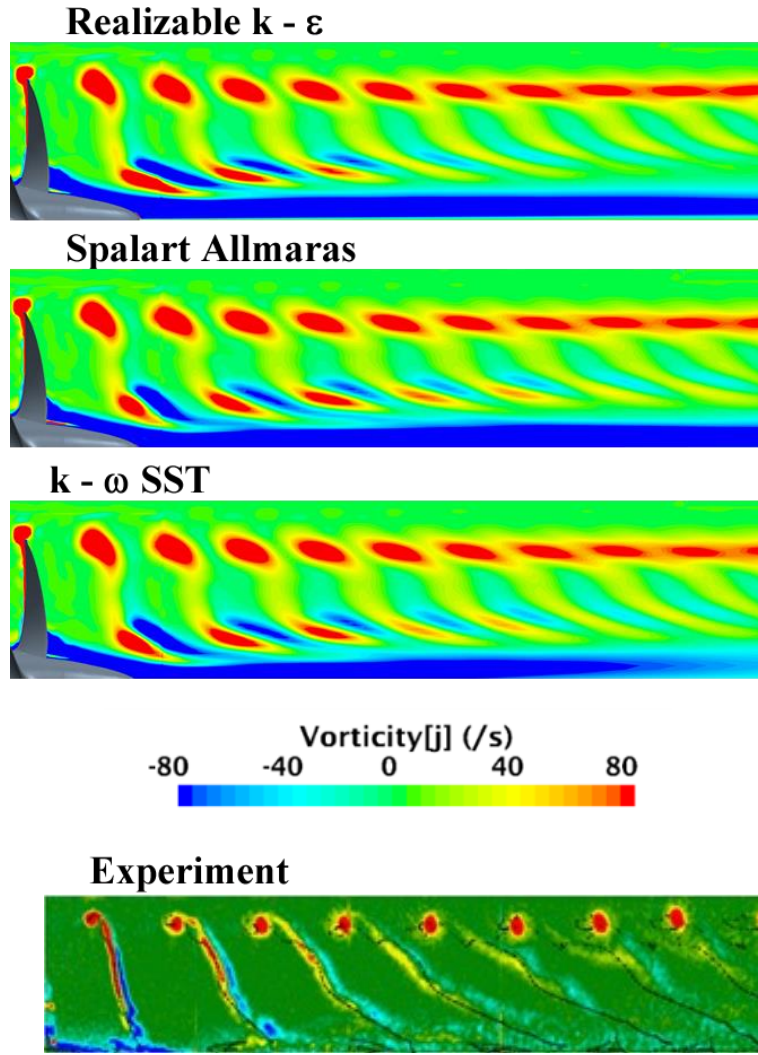
Realizable k - ε

Spalart Allmaras

k - ω SST

Vorticity[j] (/s)

| -80 | -40 | 0 | 40 | 80 |

Experiment

Figure 4. Comparison of vorticity in the Y direction (ω_Y) with the experiment.

The general view of the vorticity distribution in the propeller's slipstream is given in Figure 5. The coherent vortical structures in the propeller's slipstream was visualised using the Q criterion, which shows the vorticity regions where the vorticity magnitude is higher than the magnitude of strain rate. Q criterion is the 2nd invariants of the velocity gradient tensor and calculated with the following formulation;

$$Q = 1/2[(|\Omega|^2 - |S|^2)] \tag{13}$$

where S and Ω is the symmetric and antisymmetric component of velocity gradient (i.e. ∇u). Figure 5 is coloured by helicity by using the following formulation;

$$H = V_r\Omega/(|V_r||\Omega|) \tag{14}$$

where V_r is the relative velocity vector in the rotating reference frame. Helicity indicates the cosine angle between the absolute vorticity vector and the corresponding velocity. Helicity becomes ± 1 in the vortex core, and the sign shows the direction of swirl.

The threshold value of the Q criterion (i.e. Q_c=500) was determined using the time derivative of the pressure as the visualisation of the vorticity structures in the propeller's slipstream is dependent on the selection of Q criterion value. Therefore, using the time derivative of the pressure might be an effective way for vortex visualisation studies. The detailed information about the vortex visualisation can be found in Sezen et al. (2020).

The helices, which is mainly formed by tip vortices, remain almost at constant radius through the downstream of the propeller in Figure 5. As can be seen in Figure 5, tip and hub vortices in the propeller's slipstream were predicted slightly different by using different turbulence models. As the blade loading is low (i.e. J=0.88), significant destabilisation (or instability) of the vortex structures is not present at the tip and hub vortex in compliance with the experimental findings of Felli et al., 2011. It must be noted that tip vortices can be maintained much further downstream by using more advanced models (e.g. DES and LES).
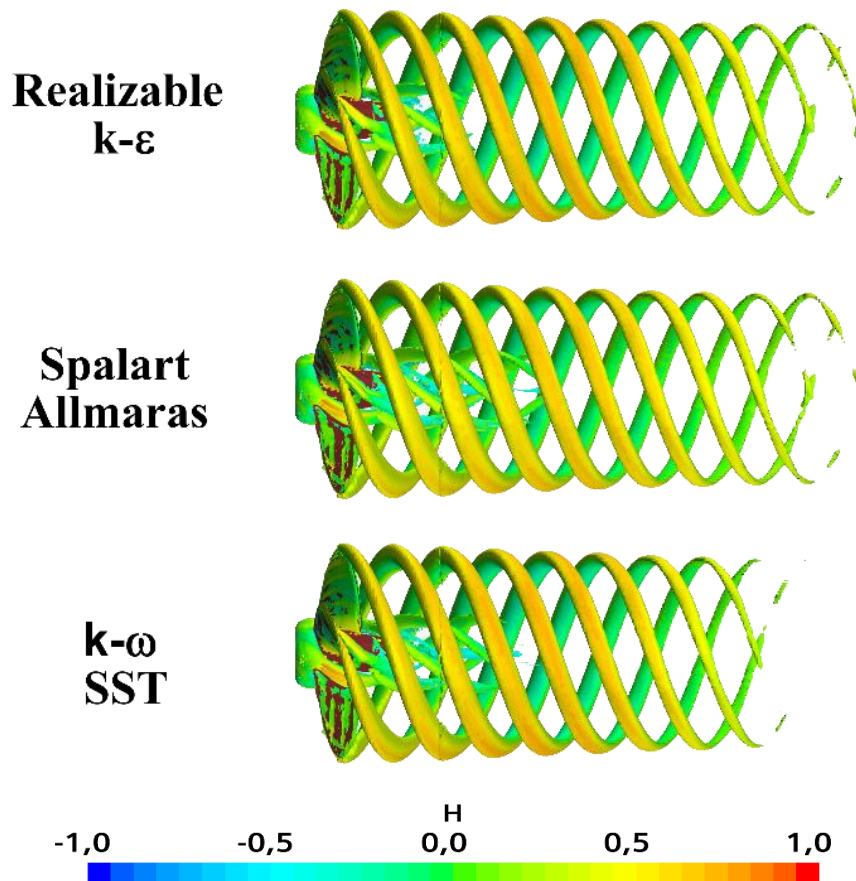
Figure 5. Comparison of tip and hub vortex in the propeller's slipstream
at J=0.88 $(Q_c = 500)$

Further detailed flow investigation was conducted at four different planes, which were located near, intermediate and far fields of the propeller's slipstream. The locations of the planes are given in Figure 6.
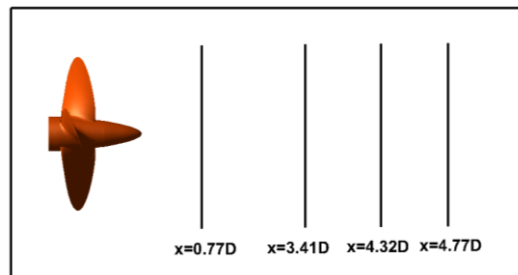
Figure 6. Representation of plane locations (Figure is not scaled).

Figure 7 shows the longitudinal view of the non-dimensional axial velocity distributions at different locations. As can be seen in Figure 7, the visual inspection of axial velocity does not present any out-of-phase unsteadiness and it shows almost uniform behaviour at different locations for all turbulent models. Hence, it can be considered that the velocity field around the propeller was predicted similarly using different turbulence models.
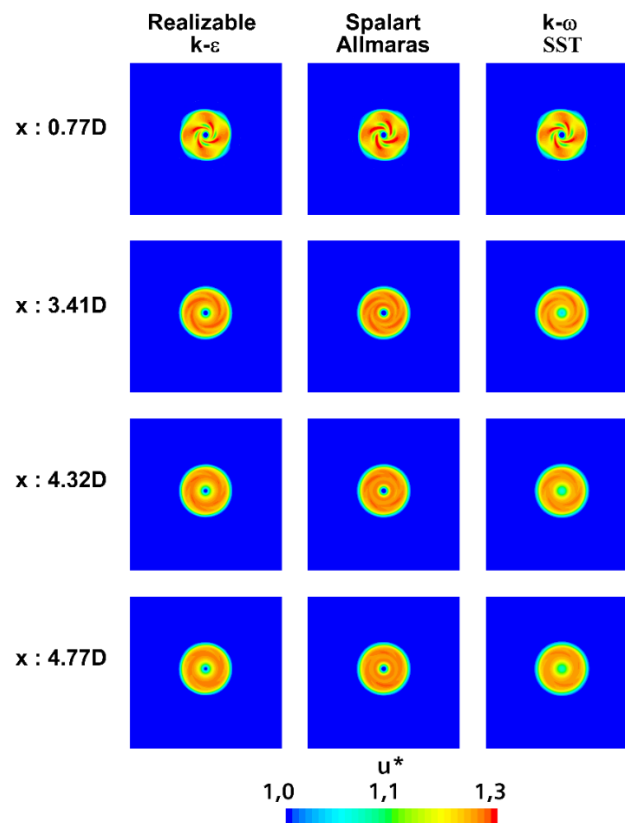
Figure 7. Comparison of non-dimensional axial velocity distributions at different sections in the propeller's slipstream at J=0.88.

Variation of turbulent viscosity ratio (TVR), which is also known as eddy viscosity ratio, is given in Figure 8 for different turbulence models. TVR is the ratio between turbulent viscosity (μ_t) and molecular dynamic viscosity (μ). Besides, turbulence viscosity (eddy viscosity) can be considered as the contribution of turbulence to the mean momentum equation. Generally speaking, turbulence is expected to increase at the flow regions where velocity changes occur. Due to the strong vortex structures, velocities and its components are high in the propeller's slipstream. Thus, vortex structures cause a change in velocity, pressure and TVR in the vortex. Computation of TVR in the vortex depends on the turbulence model and its mathematical background. Even though similar coherent vortex structures in the propeller's slipstream are predicted at J=0.88 with different turbulence models (see Figure 5), TVR levels are found dissimilar in Figure 8. As can be seen in Figure 8, TVR is small in the near field of the propeller's slipstream, but its magnitude increases rapidly for Realisable k-ε and k-ω SST turbulence models in the far-field of the propeller's slipstream. Besides, TVR presents nearly stable behaviour after near field of the propeller's slipstream (i.e. x/D=0.77) due to the consistent tip vortex structure at J=0.88. Consequently, TVR was small in the Spalart-Allmaras turbulence model, while the Realisable k-ε turbulence model produced the highest TVR.
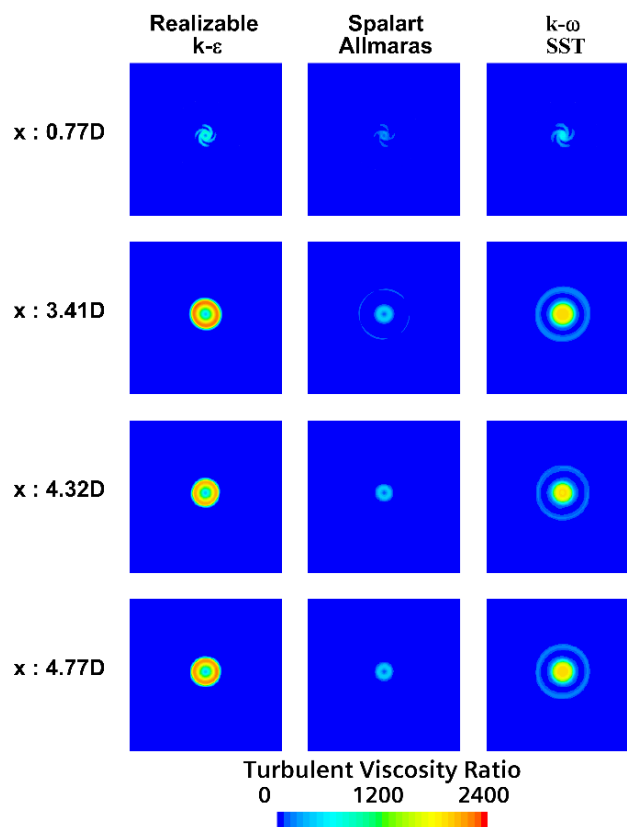

Figure 8. Comparison of TVR at J=0.88

5.2.2 J=0.3

High propeller loading condition (i.e. J=0.3) was selected to investigate the capabilities of turbulence models to follow the onset of the instability process in the propeller's slipstream. It should be noted that experimental vorticity distribution is not available at J=0.3. The vorticity distribution in the Y direction (ω_Y) can be seen in Figure 9 for different turbulence models. As can be seen in Figure 9, the instability process of the tip vortex initiates with an increase of blade loading. Tip vortices start to deform from the helical path, and the break-up process develops in the far-field of the propeller's slipstream, particularly for Realisable k-ε and Spalart-Allmaras turbulence models. Furthermore, the break-up of vortices in the Spalart-Allmaras turbulence model is more pronounced and extends towards far-field of the propeller's slipstream. The destabilisation of the tip vortex may play a role in the instability process of the hub vortex. Same remarks were also given in the comprehensive experimental study of Felli et al. (2011). Besides, the k-ω SST turbulence model smoothes out the vortex/vortex interactions and does not show any pronounced instability in comparison to other turbulence models. Similar comments for the k-ω SST turbulence model can be found in the study of Guilmineau et al. (2015).
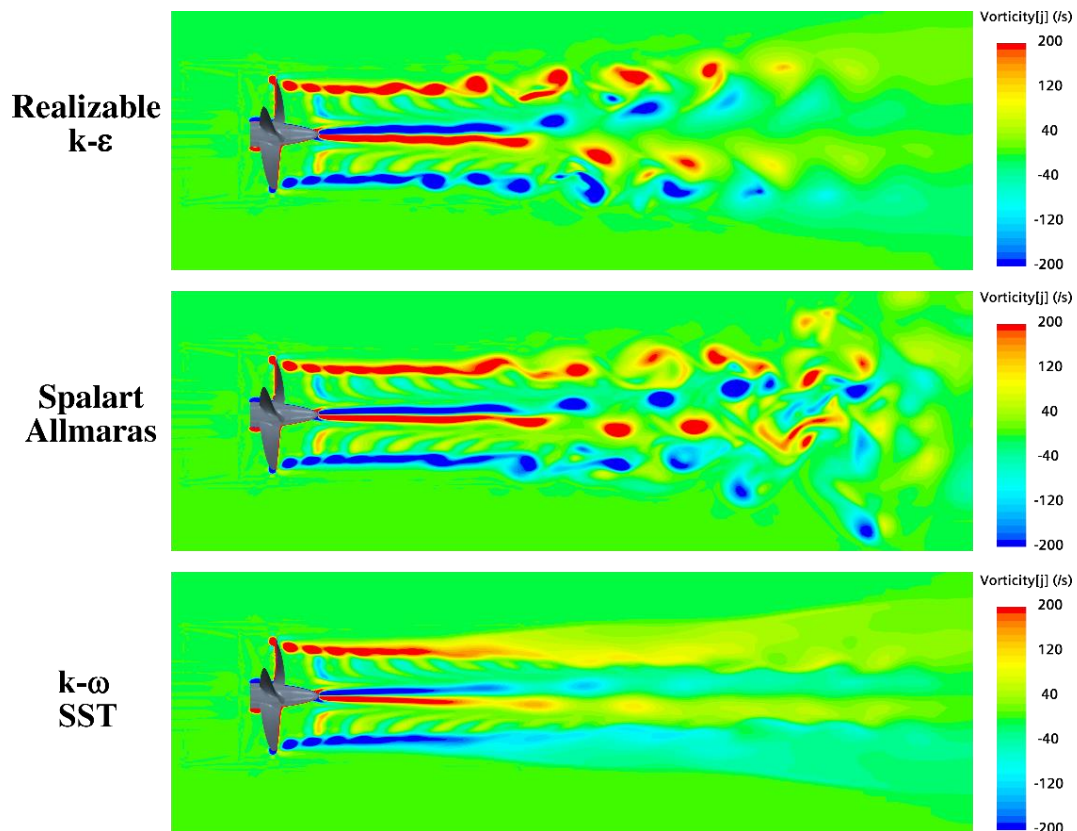

Figure 9. Comparison of vorticity distributions in the Y direction (ω_Y) at J=0.3.

The general view of the vortex structures in the propeller's slipstream is given in Figure 10. The vortex characteristics show rapid deformation in the propeller's slipstream, and more intense tip vortices occur in comparison to J=0.88 for all turbulence models. Although the tip vortices are stronger at J=0.3 than J=0.88, it extends to the short distance before the instability process occurs. Tip vortices combine and form a larger vortex with adjacent trailing vortices in the far-field of propeller's slipstream. The contraction ratio of tip vortex trajectory at J=0.3 was found to be higher than J=0.88.
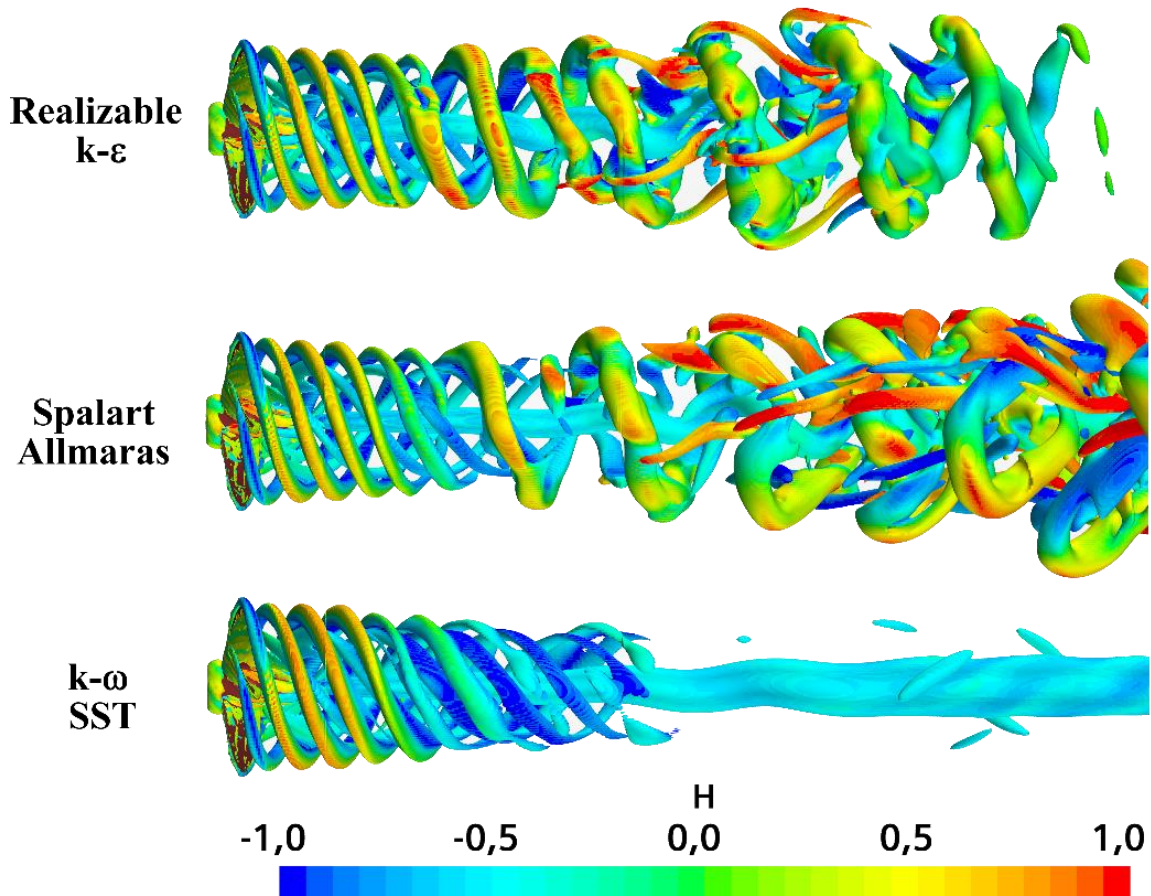
Figure 10. Comparison of tip and hub vortex in the propeller's slipstream

at J=0.3 ($Q_c = 1500$)

Vortices create different velocity and pressure fields at its surroundings and dominate the turbulent flow due to its chaotic motions and coherent structures (Hunt et al., 1988). Thus, as the tip vortex is the dominant parameter to identify the pressure field in the propeller's slipstream, break-up mechanism considerably affects the pressure or velocity variations in the flow region (Felli et al., 2006; Jang et al., 2001). Figure 11 shows the non-dimensional axial velocity distributions at near and far-field of the propeller's slipstream. Unlike the low loading condition (i.e. J=0.88), strong vortex structures, which were detected by Realisable k-ε and

Spalart-Allmaras turbulence models, deteriorate the homogenous distribution of axial velocity in the far-field of the propeller's slipstream.

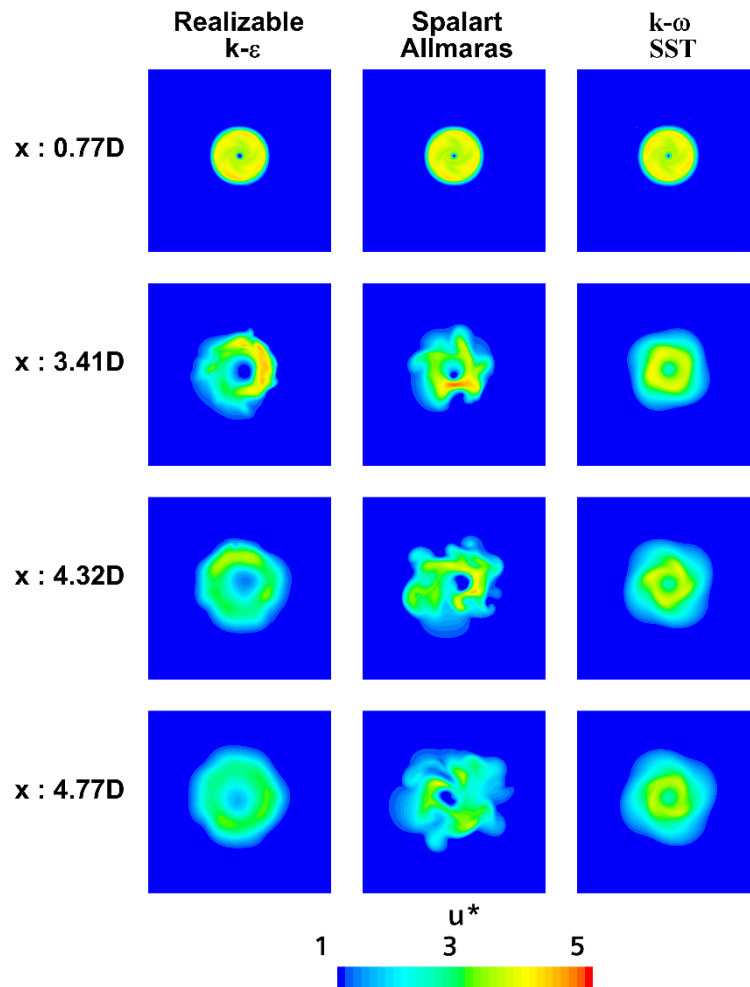Figure 11. Non-dimensional axial velocity distributions at different sections in the propeller's slipstream at J=0.3

With an increase of blade loading, the instability process caused by break-up mechanism triggers TVR, which results in the rapid growth of TVR in the far-field of the propeller's slipstream. Figure 12 shows the change of TVR with different turbulence models at different locations. As can be seen in Figure 12, Realisable k-ε produces the highest level of TVR, while the lowest level of TVR is found in the Spalart-Allmaras turbulence model. Similar to J=0.88, TVR is small in the near field of the propeller's slipstream, whereas it increases further downstream of the propeller. Similar findings can also be found in the studies of Guilmineau et al., 2015; Kumar and Mahesh, 2017.
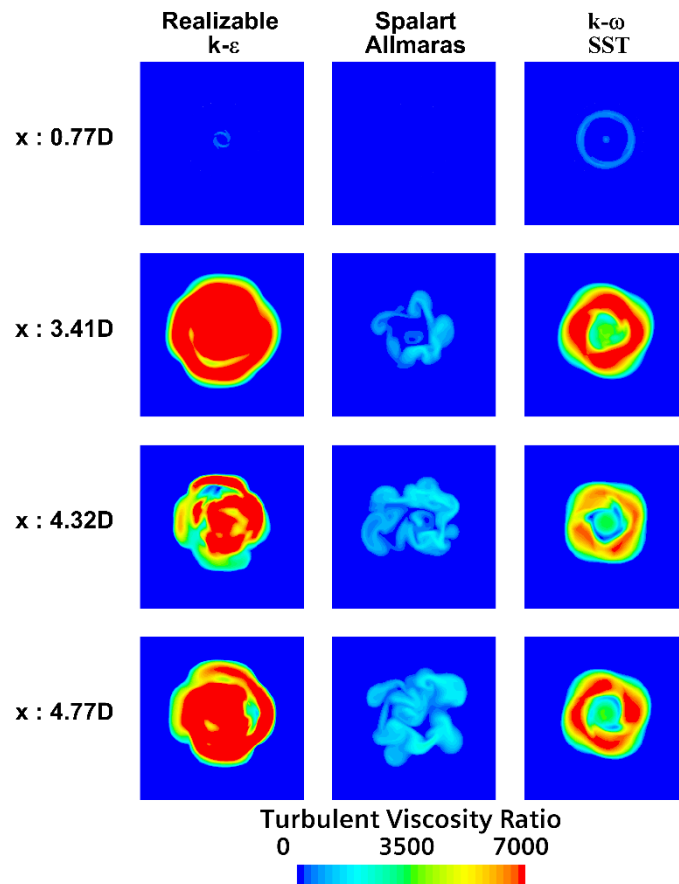
Figure 12. Comparison of TVR at J=0.3

6. Hydroacoustic Results

In this section, hydroacoustic results are presented at J=0.88 and J=0.3, respectively both in near and far-fields.

6.1   J=0.88

6.1.1   Near Field

Figure 13 shows the receiver locations in the near field of the propeller. The receiver locations are also given in Table 5. It should be noted that the coordinate system (i.e. origin) is located at the centre of propeller blades.
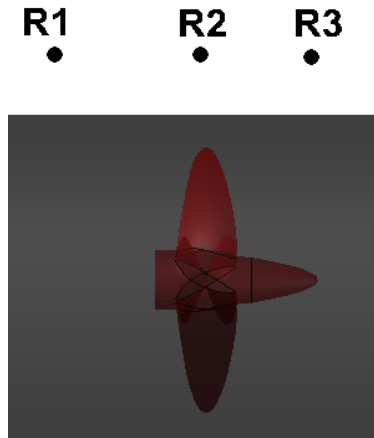
Figure 13. Representation of near-field receivers (Figure is not scaled).

Table 5. Location of near- field receivers.

Receiver	X (m)	Y (m)	Z (m)
1	0.1403		
2	0	0	0.2648
3	-0.1279		

Hydrodynamic and hydroacoustic pressures should be compatible with each other in the near field for reliable assessment of the propeller URN in the far-field. Thus, when the receivers are located proximity of the propeller where the incompressible assumption is not visible, hydrodynamic pressures can be compared with the hydroacoustic pressures. Hydrodynamic pressures are directly calculated from the solution of the Navier-Stokes equation, whereas hydroacoustic pressures are obtained by using the acoustic analogy.

Figure 14 shows the comparison of hydrodynamic and hydroacoustic pressures at Receiver 1 located upstream of the propeller. The calculated hydrodynamic pressures are given in Figure 14A by using different turbulence models, whereas the hydroacoustic pressures are presented in Figure 14B. As can be seen in Figures 14A and 14B, hydrodynamic and hydroacoustic pressures show the same amplitude and deeply characterised by BPF (Blade Passage Frequency) of the four-bladed model propeller. The comparison of hydrodynamic and hydroacoustic pressures are also given in Figure 14C. The agreement between the two pressure fluctuations is quite good. Hence, hydrodynamic pressure may be used to predict the propeller hydroacoustic performance instead of hydroacoustic pressure at Receiver 1 regardless of the turbulence model. Furthermore, due to the lack of experimental hydroacoustic results for the benchmark propeller, numerical results are compared with another numerical study in the literature presented by Ianniello et al. (2013) using RANS with

the FW-H equation in Figure 14D. As can be seen in Figure 14D, the numerical results are in good agreement with those of Ianniello et al. (2013).
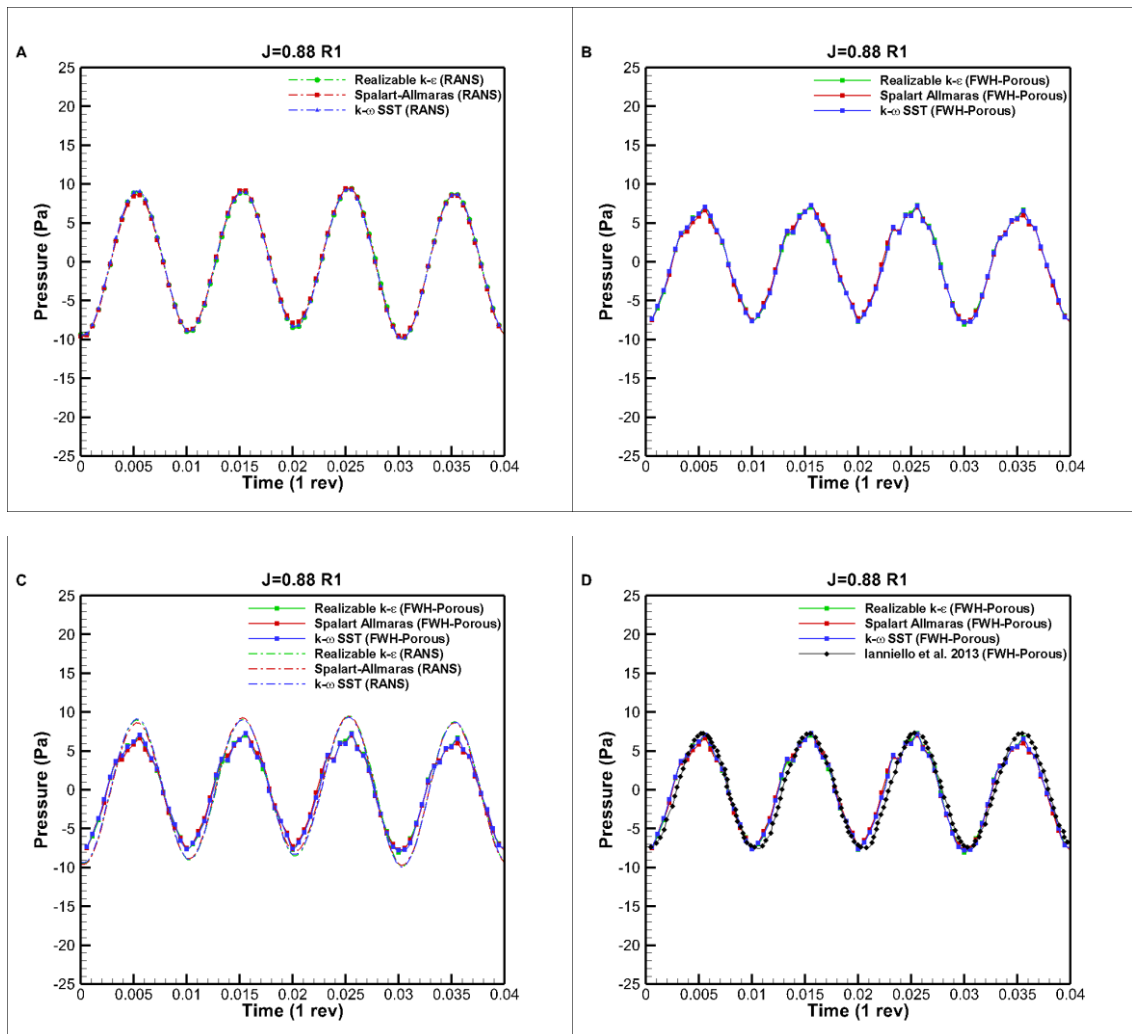

Figure 14. Comparison of hydrodynamic and hydroacoustic pressures at Receiver 1 (J=0.88).

Figure 15 shows the comparison of hydrodynamic and hydroacoustic pressures at Receiver 2, located on the propeller plane. Akin to the previous receiver location, the linear contribution of the FW-H terms are more dominant, and pressures are characterised purely by BPF. The amplitude of the signal is higher due to the contribution of blade harmonics in comparison to Receiver 1. Figure 15A and Figure 15B show the hydrodynamic and hydroacoustic pressures for three different turbulence models. Similar to Receiver 1, hydrodynamic and hydroacoustic pressures are in quite good agreement with each other. The comparison between present numerical results and those of Ianniello et al. (2013) shows a good agreement at this Receiver location (Figure 15D).
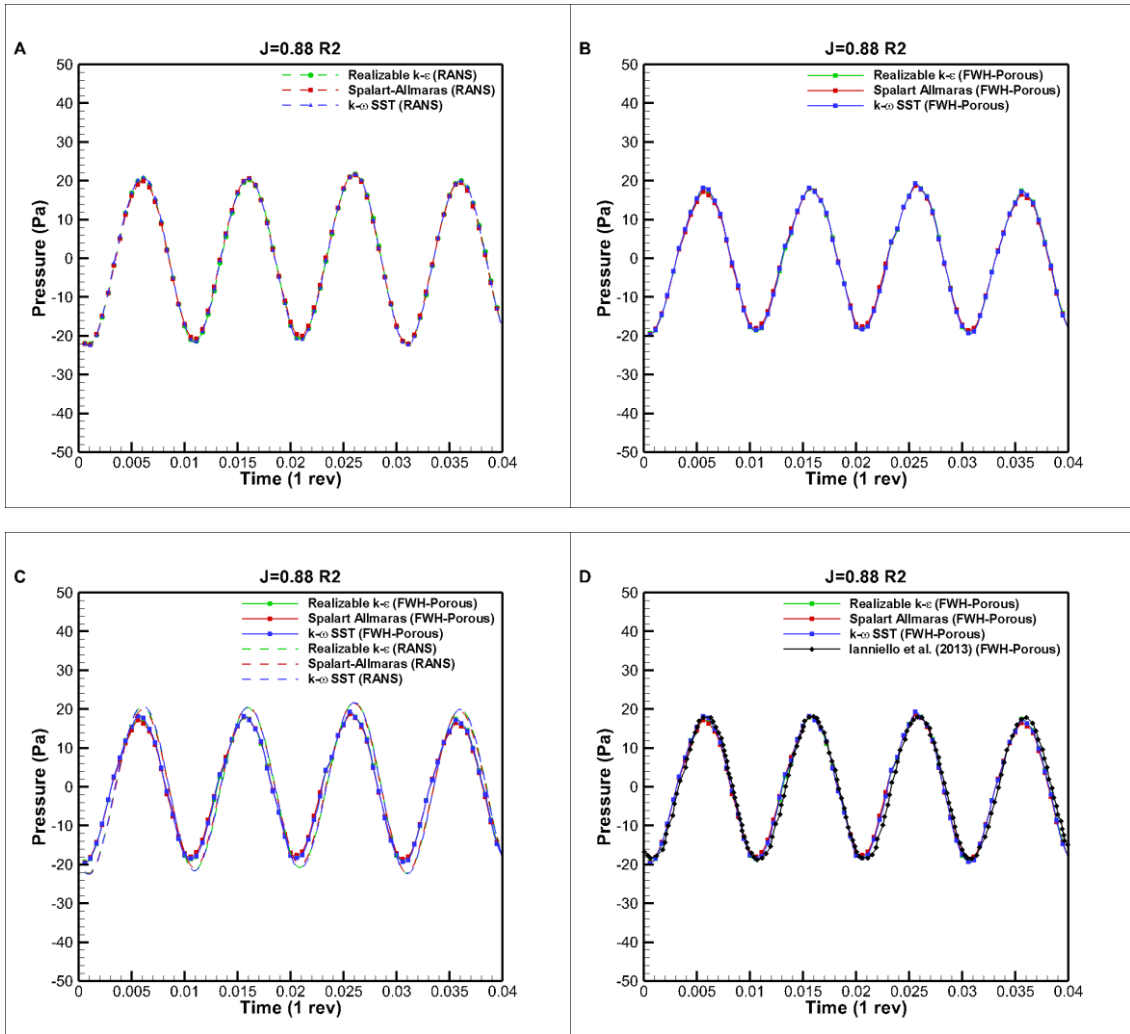
Figure 15. Comparison of hydrodynamic and hydroacoustic pressures at Receiver 2 (J=0.88).

Hydrodynamic and hydroacoustic results are also compared at Receiver 3 located downstream of the propeller. As Receiver 3 is still close to the propeller, overall shape of the acoustic signal is dominated by the contribution of the linear noise terms. Figure 16A and Figure 16B show hydrodynamic and hydroacoustic pressures for three different turbulence models at Receiver 3, whereas Figure 16C indicates the comparison of these pressures. The agreement between hydrodynamic and hydroacoustic pressures is satisfactory with a minimal phase shift. Despite the fact that the location of the Receiver 3 is nearly symmetrical with the Receiver 1, pressure fluctuations compared to Receiver 1 decreased from ∓ 8 to ∓ 5. In Figure 16D, numerical results at Receiver 3 are found to be slightly lower than those of Ianniello et al. (2013) in Figure 16D.
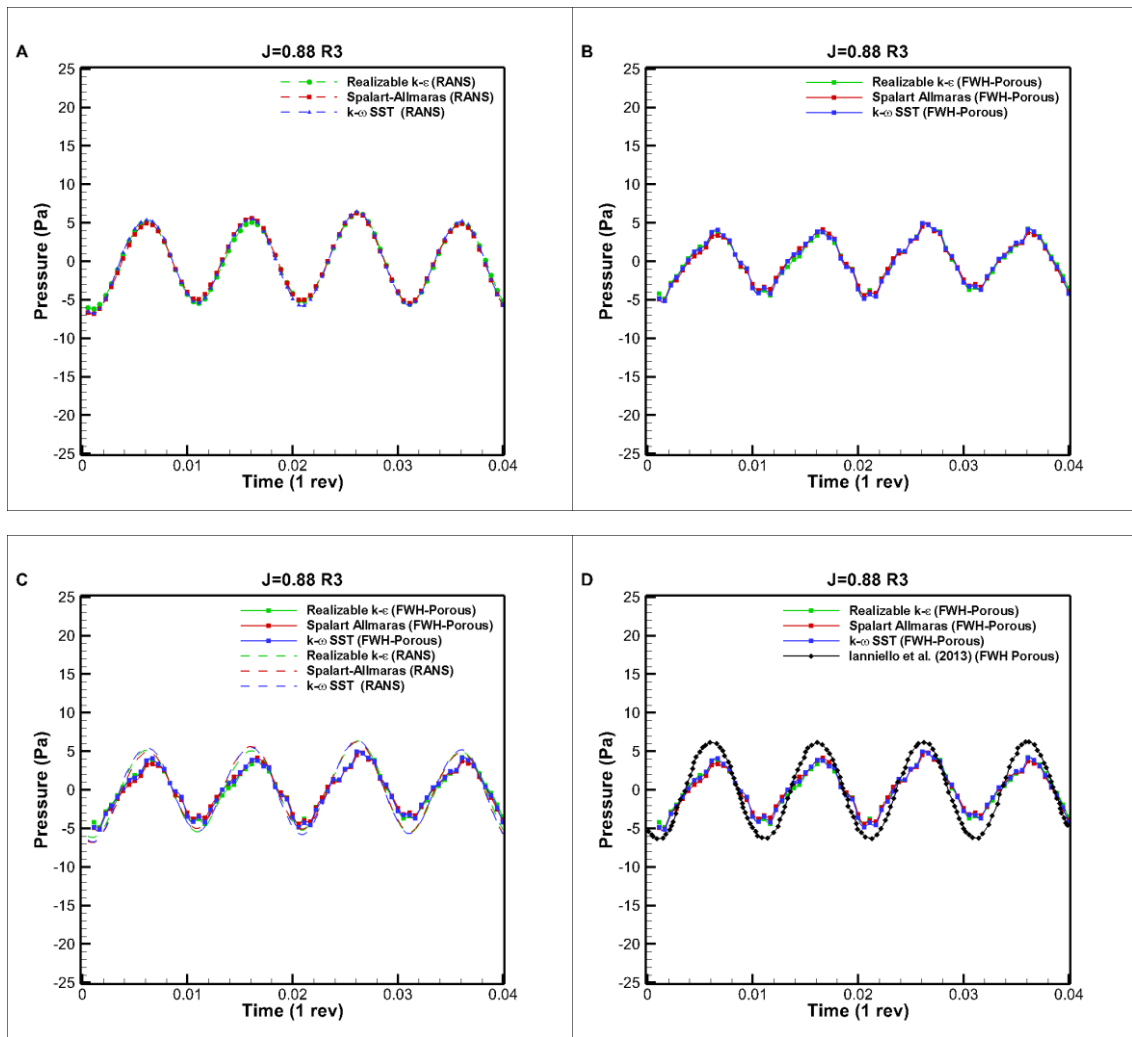
Figure 16. Comparison of hydrodynamic and hydroacoustic pressures at Receiver 3 (J=0.88).

Numerical results in the near field indicate that hydrodynamic and hydroacoustic pressures are in good agreement with each other for different turbulence models at J=0.88. Therefore, as stated in several studies in the literature (Ianniello et al., 2013; Lloyd et al., 2015b), hydrodynamic pressures might be used instead of hydroacoustic pressures in the vicinity of the propeller. However, as far away from the noise source (i.e. propeller), hydrodynamic pressures are prone to be affected by numerical dissipation which is associated with the grid resolution. Thus, FW-H analogy must be adopted in the far-field for accurate prediction of propeller URN.

6.1.2 Far Field

Three arrays of receivers were placed outside of the computational domain at a distance of 25D, 100D and 200D from the propeller's blade centre with an equal angular increment (i.e. 15°) to investigate the propeller URN in the far-field. In addition to this, receivers were also

located at both X, Y and Z-axis. The location of the receivers at the propeller plane (i.e. X-axis) can be seen in Figure 17. In the literature, FW-H acoustic analogy has been generally used with the hydrodynamic solver to predict the propeller URN in the near field to compare hydroacoustic and hydrodynamic pressures. However, one of the main reasons for the application of FW-H acoustic analogy with any incompressible solver is to predict URN in the far-field. Therefore, investigation of propeller URN in the far-field would give an insight into strong debates for the application of acoustic analogy.
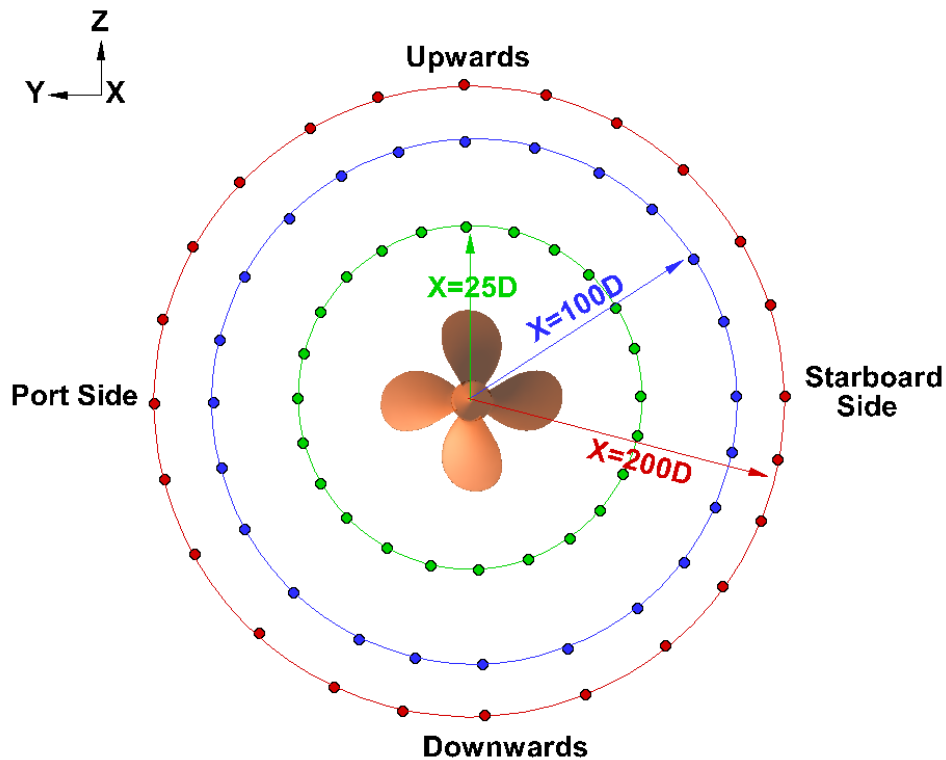

Figure 17. Representation of far-field receivers at 25D, 100D and 200D at X-axis (Figure is not scaled).

Overall acoustic pressures are calculated in time-domain and transferred to the frequency domain by using Fast Fourier Transform (FFT) for each receiver. Sound Pressure Level (SPL) can be calculated by using the following equation;

$$SPL = 20\log\left(\frac{p_{rms}}{p_{ref}}\right) \qquad (15)$$

Here, p_{rsm} is the acoustic pressure; Pa, p_{ref} is the reference pressure and 10^{-6}Pa for water. Figure 18 indicates directivity patterns predicted by using FW-H acoustic analogy together with three different turbulence models at the propeller plane (i.e. 25D, 100D and 200D). It was found that predicted noise results have symmetry pattern from 0° to 360°. Besides, the numerical results show that acoustic analogy which is coupled with different turbulence

models predicts the same noise directivity pattern regardless of the distance at low loading conditions (i.e. J=0.88). As explained in Section 5 (see Figure 8), the magnitude of TVR is smaller in the Spalart-Allmaras turbulence model in comparison to Realisable k-ε and k-ω SST turbulence models. However, vortices and its extensions are predicted similarly by different turbulence models in the propeller's slipstream (see Figure 4 and 5). Hence, vorticity can be considered as the dominant non-linear noise source and characterise the overall acoustic pressure.
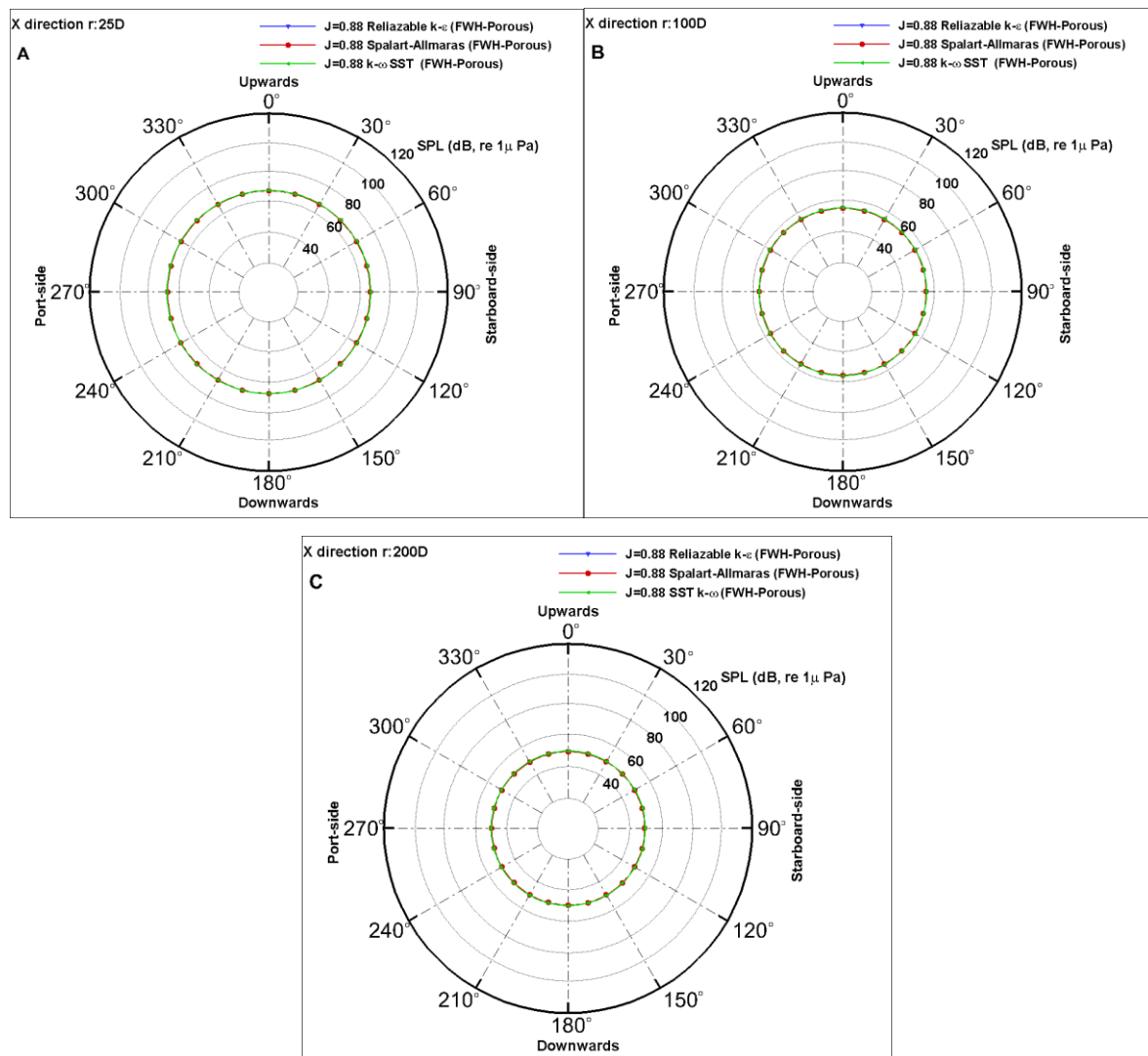

Figure 18. Noise directivity predicted at J=0.88 (A: 25D, B:100D and C:200D)

On the other hand, noise levels can be extrapolated to the desired distance by using ITTC distance normalisation formulation, which is given below; (ITTC, 2014a)

$$SPL_{ITTC} = SPL + 20\log\left(\frac{d}{d_{ref}}\right) \qquad (16)$$

In this formulation, SPL_{ITTC} is the extrapolated noise level at the desired distance, SPL is the measured noise level at the reference distance, d is the receiver distance from the noise source and d_{ref} is the reference distance. ITTC (ITTC, 2014a) formulation is generally applied in the experimental facilities to transfer the measured value from the confinement region to free field conditions. As clearly stated in our previous study (Sezen and Kinaci, 2019), extrapolation of the noise results from the near field to the far-far field by the aid of ITTC distance formulation does not yield satisfactory results for far-field noise predictions. Therefore, it has been suggested that near field noise results should not be extrapolated to far-field for reliable far-field noise predictions. However, in this study, ITTC distance formulation can also be used for the extrapolation of the numerical results from far-field to far-field. In this regard, URN results predicted with k-ω SST turbulence model at 25D and 180° can be taken as a reference result and extrapolated to 100D and 200D by using ITTC distance formulation. Table 6 shows the numerical results for both reference and extrapolated data. As can be seen in Table 6, unlike the extrapolation of URN results from near field to far-field, ITTC distance formulation can be reliably used for the extrapolation of noise results from far-field to far-field. It should be noted that this inference is valid at every receiver position and different turbulence models in Figure 18.

Table 6. Extrapolated and predicted noise results at 25D and 180° (J=0.88)

Receiver	SPL_{FWH} (dB)	SPL_{ITTC} (dB)	Difference %
25D	68.26	-	-
100D	56.21	56.22	0.02
200D	50.18	50.20	0.02

6.2   J=0.3

6.2.1   Near Field

The hydroacoustic analysis was conducted at J=0.3. As expected, an increase of the blade loading causes an increase in propeller URN inevitably. The main features of vorticity field in the propeller's slipstream remarkably change due to the rapid increase of hydrodynamic gradients between the face and back sides of the propeller blade at J=0.3 (see Figures 5 and 10).

Similar to the previous advance coefficient (i.e. J=0.88), hydrodynamic and hydroacoustic pressures are compared for the receivers (see Figure 13) located around the propeller in Figure 19. Figure 19A and 19B show hydrodynamic and hydroacoustic pressures at Receiver 1, respectively. The hydrodynamic and hydroacoustic pressures are found to be a

satisfactorily good agreement for three turbulence models (Figure 19C). Besides, pressure fluctuations increase approximately from ∓8 to ∓18 at Receiver 1 in comparison to J=0.88 due to the higher blade loading (see Figure 14).

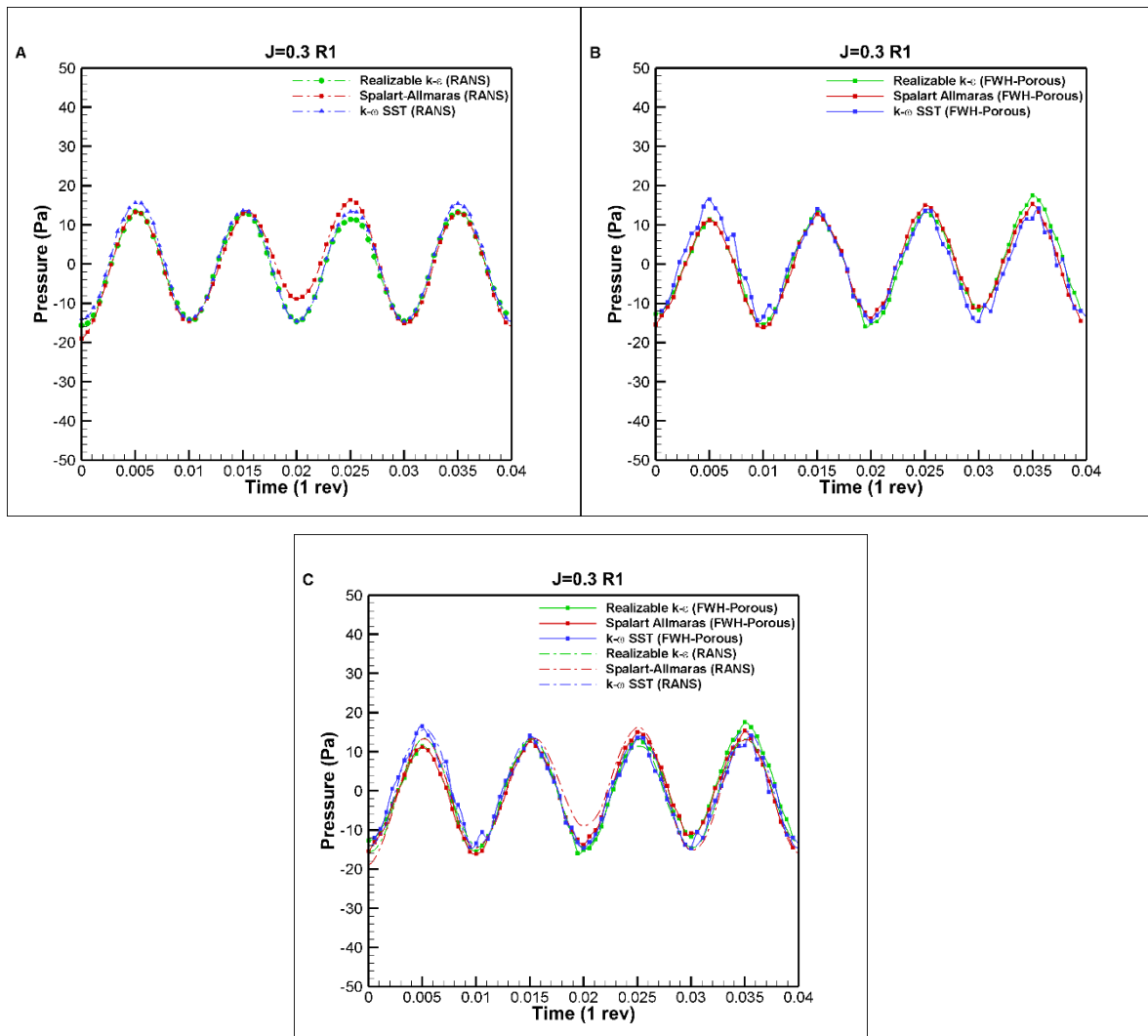Figure 19. Comparison of hydrodynamic and hydroacoustic pressures at Receiver 1 (J=0.3).

A similar comparison between hydrodynamic and hydroacoustic pressures was performed at Receiver 2 (see Figure 13). The hydrodynamic and hydroacoustic pressures are characterised by BPF due to the higher contribution of linear noise terms at Receiver 2 (Figure 20A and Figure 20B). The agreement between hydrodynamic and hydroacoustic pressures is quite good for all turbulence models (Figure 20C). As expected, the amplitude of the pressure fluctuations increases in comparison to J=0.88 at Receiver 2. Having said that present hydroacoustic results are compared with those of Ianniello et al. (2013) in Figure 20D and good agreement is found.
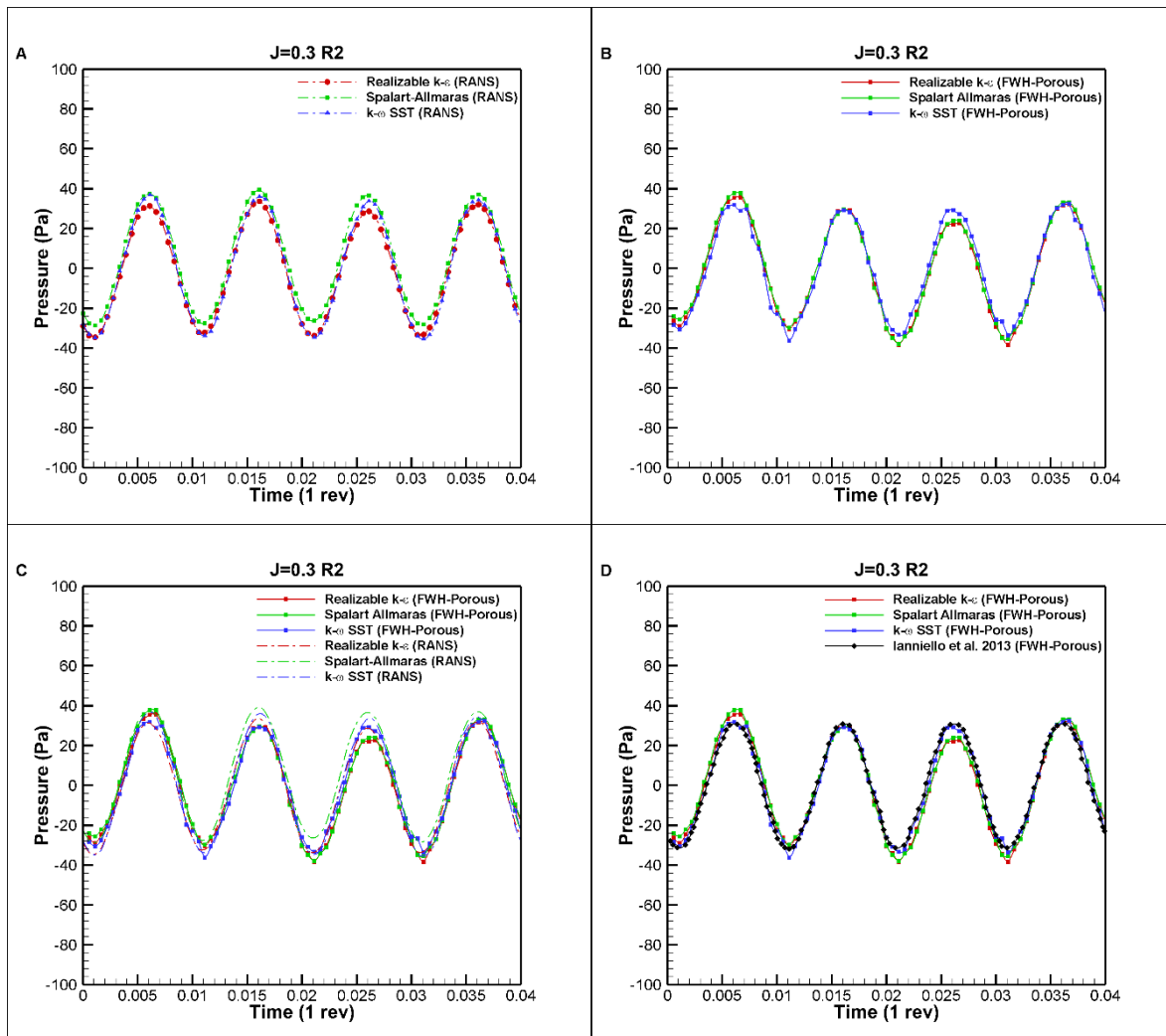
Figure 20. Comparison of hydrodynamic and hydroacoustic pressures at Receiver 2 (J=0.3).

6.2.2 Far Field

Noise directivity of the propeller is presented under high loading condition in Figure 21. Unlike the low loading condition (i.e. J=0.88), hydroacoustic results notably change by using different turbulence models at J=0.3 in Figure 21. The reason behind this is that flow details in the propeller's slipstream (i.e. vorticity, turbulence, and velocity) is predicted in a different way by turbulence models, which lead dissimilar prediction of propeller URN. As aforementioned in Section 5, the Spalart-Allmaras turbulence model calculates a small amount of TVR in the propeller's slipstream, whereas higher TVR is calculated by Realisable k-ε and k-ω SST turbulence models. Besides, vortical structures are predicted in a different manner by turbulence models. The increased blade loading triggers the instability process, which results in break-up of the vortices in the propeller's slipstream (see Figure 10). As explained in Section 5, the k-ω SST turbulence model fails the capture the instability process similar to Realisable k-ε and Spalart-Allmaras turbulence models and smoothes out the

vorticity field rapidly (see Figure 10). Thus, propeller URN levels are predicted differently by turbulence models because of the differences for capturing the instability process. The acoustic analogy, which is coupled with the Spalart-Allmaras turbulence model predicts high URN in comparison to other models. As can be seen in Figure 21, the difference between the overall noise levels predicted by using the Spalart-Allmaras turbulence and k-ω SST models is around 10-15 dB. In contrast, 2-3 dB noise differences are found between the Spalart-Allmaras and Realisable k-ε turbulence models. Similar to J=0.88, ITTC distance formulation gives compatible results for the extrapolation of the results from far-field to far-field at low loading conditions by using different turbulence models which are coupled with an acoustic analogy. It should be noted that the considerable differences in terms of the overall SPL between J=0.8 and J=0.3 originate from the prediction of SPL at sub-harmonics in the far-field. When considering the general noise spectrum (i.e. SPL-f), the differences between noise levels decrease at each discrete frequency, especially after 3rd BPF.
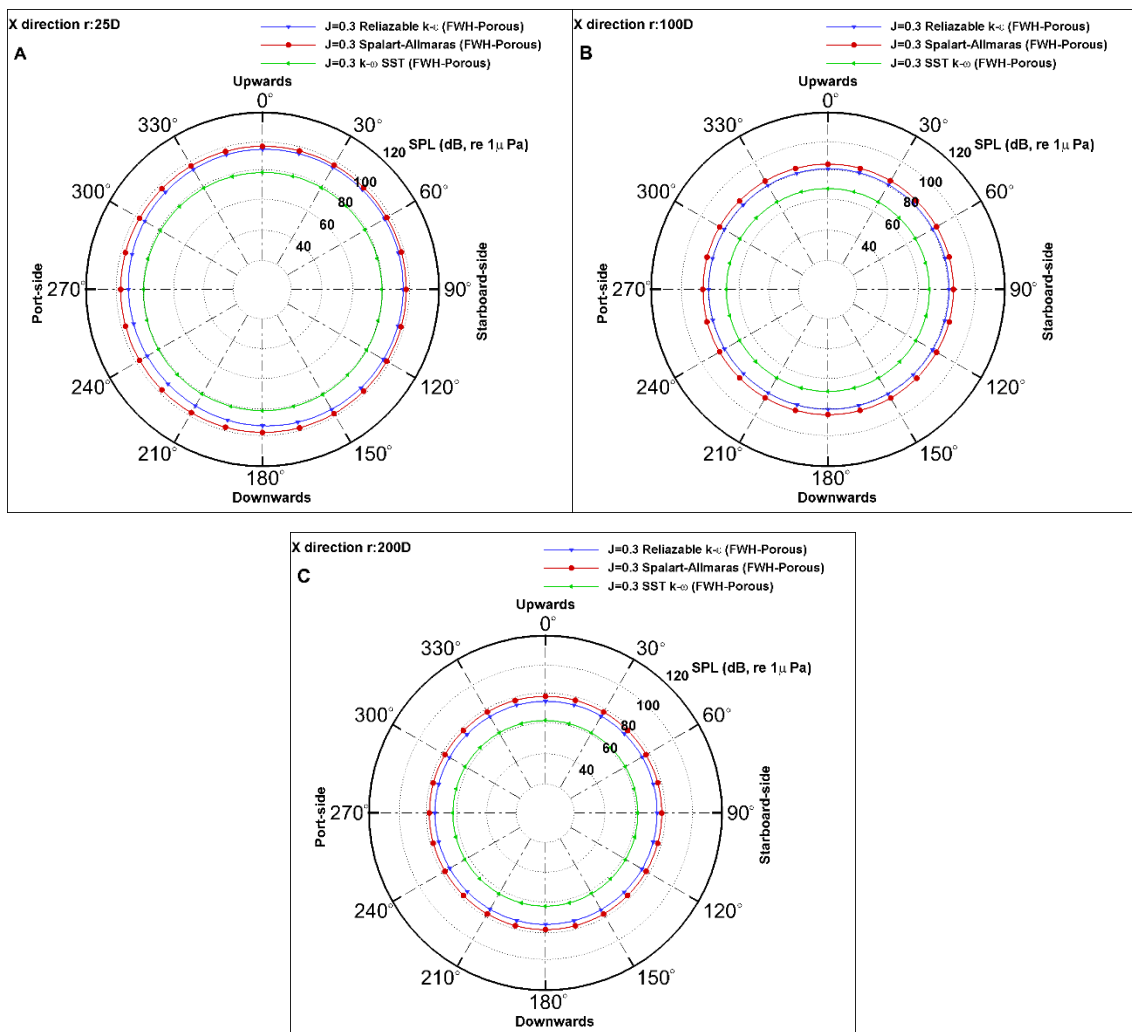
Figure 21. Noise directivity of the propeller at J=0.3 (A: 25D, B:100D and C:200D)

7. Concluding Remarks

In this study, capabilities of different eddy viscosity turbulence models together with the acoustic analogy were investigated for the prediction of marine propeller hydrodynamic and hydroacoustic performance under non-cavitating conditions. The numerical results reveal crucial points for the prediction of propeller URN using RANS based hybrid methods. The consequences of the study can be summarised as in below;

- With an increase of the blade loading, the flow properties in the propeller's slipstream significantly changed. In particular, the instability process of the vorticity field started, and it consequently resulted in a break-up mechanism in the far-field of the propeller` slipstream. The k-ω SST turbulence model failed to capture the break-up mechanism when compared to other turbulence models.

- Akin to similar studies in the literature, hydrodynamic and hydroacoustic pressures were found in a good agreement with each other in the near field. Thus, the reliability of the numerical solution was proved for far-field noise predictions where hydrodynamic pressures are not available.

- Numerical results showed that ITTC distance formulation could be reliably used for the extrapolation of the noise levels from far-field to far-field.

- URN results indicated the underwater pressure field seems to be significantly affected in the presence of the vortex instability. Thus, vortex instabilities or break-up mechanism as a non-linear noise source might be the main contributor to the overall acoustic pressure.

- The results suggested that the selection of the turbulence model is depended on the operating condition for the prediction of propeller URN. Three different turbulence models which are coupled with porous FW-H equation predicts the propeller URN similarly at low loading condition. In contrast, the k-ω SST turbulence model together with porous FW-H equation underpredicted the propeller URN at high loading condition in comparison to other turbulence models.

- It should be noted that the present RANS based hybrid method can only be used for the prediction of propeller URN, especially in the preliminary design stage. Therefore, scale resolving simulations (i.e. DES or LES) should be used with porous FW-H equation

for more in-depth studies as the flow details such as vorticity field, instability process, etc. are predicted more accurate than RANS solver.

Acknowledgements

References

Abe, K., Kondoh, T., Nagano, Y., 1994. A new turbulence model for predicting fluid flow and heat transfer in separating and reattaching flows-I. Flow field calculations. Int. J. Heat Mass Transf. 37, 139–151. https://doi.org/10.1016/0017-9310(94)90168-6

Baek, D.G., Yoon, H.S., Jung, J.H., Kim, K.S., Paik, B.G., 2015. Effects of the advance ratio on the evolution of a propeller wake. Comput. Fluids 118, 32–43. https://doi.org/10.1016/j.compfluid.2015.06.010

Bulat, M.P., Bulat, P.V., 2013. Comparison of turbulence models in the calculation of supersonic separated flows. World Appl. Sci. J. 27, 1263–1266. https://doi.org/10.5829/idosi.wasj.2013.27.10.13715

Calcagno, G., Felice, F. Di, Felli, M., Franchi, S., Pereira, F., Salvatore, F., 2006. The INSEAN E779a Propeller Test Case : a Database For CFD Validation. Proc. MARNET-CFD Final Workshop. 1–5.

Cebeci, T., 2013. Analysis of turbulent flows with computer programs, 3rd edition, Butterworth-Heinemann.

Cianferra, M., Petronio, A., Armenio, V., 2019. Non-linear noise from a ship propeller in open sea condition. Ocean Eng. 191, 106474. https://doi.org/10.1016/j.oceaneng.2019.106474

Dacles-Mariani, J., Kwak, D., Zilliac, G., 1999. On numerical errors and turbulence modeling in tip vortex flow prediction. Int. J. Numer. Methods Fluids 30, 65–82. https://doi.org/10.1002/(SICI)1097-0363(19990515)30:1<65::AID-FLD839>3.0.CO;2-Y

Davidson, L., Nielsen, P.V., Sveningsson, A., 2003. Modifications of the v^2-f model for Computing the Flow in a 3D Wall Jet, in: Proceedings of the International Symposium on Turbulence, Heat and Mass Transfer, October 12-17, 2003, Antalya,Turkey.

Di Francescantonio, P., 1997. A New Boundary Integral Formulation for the Prediction of Sound Radiation. J. Sound Vib. 202, 491–509.

Durbin, P.A., 1991. Near-wall turbulence closure modeling without "damping functions". Theor. Comput. Fluid Dyn. 3, 1–13. https://doi.org/10.1007/BF00271513

Ebrahimi, A., Razaghian, A.H., Seif, M.S., Zahedi, F., Nouri-Borujerdi, A., 2019. A comprehensive study on noise reduction methods of marine propellers and design procedures. Appl. Acoust. 150, 55–69. https://doi.org/10.1016/j.apacoust.2018.12.004

Farassat, F., 2007. Derivation of Formulations 1 and 1A of Farassat. Nasa/TM-2007-214853 214853, 1–25.

Feder, D.-F., Abdel-Maksoud, M., 2016. Tracking a Tip Vortex with Adaptive Vorticity Confinement and Hybrid RANS-LES. Open J. Fluid Dyn. 06, 406–429.

https://doi.org/10.4236/ojfd.2016.64030

Felli, M., Camussi, R., Di Felice, F., 2011. Mechanisms of evolution of the propeller wake in the transition and far fields. J. Fluid Mech. 682, 5–53. https://doi.org/10.1017/jfm.2011.150

Felli, M., Di Felice, F., Guj, G., Camussi, R., 2006. Analysis of the propeller wake evolution by pressure and velocity phase measurements. Exp. Fluids 41, 441–451. https://doi.org/10.1007/s00348-006-0171-4

Ffowcs Williams, J.E., Hawkings, D.L., 1969. Sound Generation by Turbulence and Surfaces in Arbitrary Motion. Philos. Trans. R. Soc. London. Ser. A, Math. Phys. Sci. 264, 321–342. https://doi.org/10.1098/rsta.1969.0031

Guilmineau, E., Deng, G.B., Leroyer, A., Queutey, P., Visonneau, M., Wackers, J., 2015. Influence of the Turbulence Closures for the Wake Prediction of a Marine Propeller, Fourth International Symposium on Marine Propulsors smp'15, Austin, Texas. ss. 251–256. https://doi.org/10.1007/978-3-319-63212-4_31

Hildebrand, J.A., 2009. Anthropogenic and natural sources of ambient noise in the ocean. Mar. Ecol. Prog. Ser. 395, 5–20. https://doi.org/10.3354/meps08353

Hunt, J.C.R., Wray, a a, Moin, P., 1988. Eddies, streams, and convergence zones in turbulent flows, in: Center for Turbulence Research, Proceedings of the Summer Program. pp. 193–208. https://doi.org/CTR-S88

Ianniello, S., 2015. Sheet cavitation noise prediction from a marine propeller. 22nd Int. Congr. Sound Vibration. ICSV22 12–16.

Ianniello, S., De Bernardis, E., 2015. Farassat's formulations in marine propeller hydroacoustics. Int. J. Aeroacoustics 14, 87–103. https://doi.org/10.1260/1475-472X.14.1-2.87

Ianniello, S., Muscari, R., Di Mascio, A., 2013. Ship underwater noise assessment by the acoustic analogy. Part I: Non-linear analysis of a marine propeller in a uniform flow. J. Mar. Sci. Technol. 18, 547–570. https://doi.org/10.1007/s00773-013-0227-0

IMO, M.R., 2014. Guidelines for the reduction of underwater noise from commercial shipping to address adverse impacts on marine life, MEPC.1/ Circ.833

ITTC, 2014a. Specialist Committee on Hydrodynamic Noise, Final Report and Recommendations to the 27th ITTC.

ITTC, 2014b. Specialist Committee on Hydrodynamic Noise, Written Discussion at the 27th ITTC.

Jang, C.M., Furukawa, M., Inoue, M., 2001. Analysis of vortical flow field in a propeller fan by LDV measurements and LES-Part II: Unsteady nature of vortical flow structures due to tip vortex breakdown. J. Fluids Eng. Trans. ASME 123, 755–761. https://doi.org/10.1115/1.1412566

Ji, B., Luo, X., Wu, Y., Peng, X., Xu, H., 2012. Partially-Averaged Navier-Stokes method with modified k-ε model for cavitating flow around a marine propeller in a non-uniform wake. Int. J. Heat Mass Transf. 55, 6582–6588. https://doi.org/10.1016/j.ijheatmasstransfer.2012.06.065

Kumar, P., Mahesh, K., 2017. Large eddy simulation of propeller wake instabilities. J. Fluid Mech. 814, 361–396. https://doi.org/10.1017/jfm.2017.20

Launder, B.E., Sharma, B.I., 1974. Application of the energy-dissipation model of turbulence to the calculation of flow near a spinning disc. Lett. Heat Mass Transf. 1, 131–137. https://doi.org/10.1016/0094-4548(74)90150-7

Li, D.Q., Hallander, J., Johansson, T., 2018. Predicting underwater radiated noise of a full scale ship with model testing and numerical methods. Ocean Eng. 161, 121–135.

https://doi.org/10.1016/j.oceaneng.2018.03.027

Lidtke, A.K., Lloyd, T.P., Vaz, G., 2019. Acoustic modelling of a propeller subject to non-uniform inflow. 6th Int. Symp. Mar. Propulsors, smp'19, Rome, Italy.

Lloyd, T.P., Lidtke, A.K., Rijpkema, D., Van Wijngaarden, E., Turnock, S.R., Humphrey, V.F., 2015a. Using the FW-H equation for hydroacoustics of propellers. 18th Numer. Towing Tank Symp. NuTTS'2015, Cortona, Italy.

Lloyd, T.P., Rijpkema, D.R., van Wijngaarden, E., 2015b. Marine propeller acoustic modelling: comparing CFD results with an acoustic analogy approach. 4th Int. Symp. Mar. Propulsors. smp'15. Austin, Texas.

Lloyd, T.P., Rijpkema, D.R., van Wijngaarden, E., 2014. Implementing the Ffowcs Williams and Hawkings acoustic analogy into a viscous CFD solver. 17th Numer. Towing Tank Symp. NuTTS'2014, Marstrand, Sweden.

Luo, J., Razinsky, E.H., 2008. Conjugate Heat Transfer Analysis of a Cooled Turbine Vane Using the V2F Turbulence Model. ASME Turbo Expo 2006 Power Land, Sea, Air, Am. Soc. Mech. Eng. Digit. Collect. pp. 865–875. https://doi.org/https://doi.org/10.1115/GT2006-91109

Menter, F.R., 1994. Two-equation eddy-viscosity turbulence models for engineering applications. AIAA J. 32, 1598–1605. https://doi.org/10.2514/3.12149

Morgut, M., Nobile, E., 2012. Influence of grid type and turbulence model on the numerical prediction of the flow around marine propellers working in uniform inflow. Ocean Eng. 42, 26–34. https://doi.org/10.1016/j.oceaneng.2012.01.012

Muscari, R., Di Mascio, A., Verzicco, R., 2013. Modeling of vortex dynamics in the wake of a marine propeller. Comput. Fluids 73, 65–79. https://doi.org/10.1016/j.compfluid.2012.12.003

Nitzkorski, Z., 2015. A novel porous Ffowcs-Williams and Hawkings acoustic methodology for complex geometries, PhD Thesis, The Faculty of the Graduate School of The University of Minnesota, USA.

Peng, H., Qiu, W., Ni, S., 2013. Effect of turbulence models on RANS computation of propeller vortex flow. Ocean Eng. 72, 304–317. https://doi.org/10.1016/j.oceaneng.2013.07.009

Poncet, S., Da Soghe, R. , Facchini, B., 2010. RANS Modeling Of Flow In Rotating Cavity System, in: V European Conference on Computational Fluid Dynamics, ECCOMAS CFD 2010, Lisbon, Portugal.

Pope, S.B., 2000. Turbulent Flows, Cambridge University Press.

Prandtl, L., 1949. Report on Investigation of Developed Turbulence, National Advisorory Committee for Aeronautics, NACA Technical Memorandum 1231, NACATM-1231.

Roache, P.J., 1997. Quantification of uncertainty in computational fluid dynamics. Annu. Rev. Fluid Mech. 29, 123–160. https://doi.org/10.1146/annurev.fluid.29.1.123

Ross, D., 1976. Mechanics of Underwater Noise, Pergamon, New York.

Sadrehaghighi, I., 2019. Turbulence Modeling, A Review, Report Number:1.86.9.

Salvatore, F., Streckwall, H., Terwisga, T. Van, 2009. Propeller cavitation modelling by CFD - results from the VIRTUE 2008 Rome Workshop. Proc. 1st Int. Symp. Mar. Propulsors. smp'09, Trondheim, Norway.

Salvatore, F., Testa, C., Ianniello, S., Pereira, F., 2006. Theoretical Modelling of Unsteady Cavitation and Induced Noise, 6th International Symposium on Cavitation CAV2006, pp. 1–13, Wageningen, The Netherlands.

Sengupta, T.K., Sircar, S.K., Dipankar, A., 2006. High accuracy schemes for DNS and acoustics, Journal of Scientific Computing. https://doi.org/10.1007/s10915-005-4928-3

Seol, H., Jung, B., Suh, J.C., Lee, S., 2002. Prediction of non-cavitating underwater propeller

noise. J. Sound Vib. 257, 131–156. https://doi.org/10.1006/jsvi.2002.5035

Seol, H., Suh, J.C., Lee, S., 2005. Development of hybrid method for the prediction of underwater propeller noise. J. Sound Vib. 288, 345–360. https://doi.org/10.1016/j.jsv.2005.01.015

Sezen, S., Kinaci, O.K., 2019. Incompressible flow assumption in hydroacoustic predictions of marine propellers. Ocean Eng. 186, 106138. https://doi.org/10.1016/j.oceaneng.2019.106138

Sezen, S., Yurtseven, A., Cosgun, T., Atlar, M., 2020. Numerical Investigation of Marine Propeller Underwater Radiated Noise Using Acoustic Analogy Part 1: The influence of grid resolution. Ocean Eng., paper submitted.

Shih, T.-H., Liou, W.W., Shabbir, A., Yang, Z., Zhu, J., 1995. A New Kt Eddy Viscosity Model for High Reynolds Number Turbulent Flows. Comput. Fluids 24, 227–238. https://doi.org/10.1007/978-3-319-27386-0_7

Sikirica, A., Carija, Z., Kranjcevic, L., Lucin, I., 2019. Grid type and turbulence model influence on propeller characteristics prediction. J. Mar. Sci. Eng. 7. https://doi.org/10.3390/jmse7100374

Spalart, P.R., 1999. Strategies for turbulence modelling and simulations. In Engineering Turbulence Modelling and Experiments 4, pp. 3-17, Elsevier Science Ltd.

Spalart, P.R., Allmaras, S.R., 1992. A One-Equatlon Turbulence Model for Aerodynamic Flows. American Institute of Aeronautics and Astronautics, 30th Aerospace Sciences Meeting and Exhibit, 6-9 January 1992, Reno, NV, USA. doi: 10.2514/6.1992-439.

StarCCM+, 2019. User Guide.

Sundén, B., Fu, J., 2017. Heat transfer in aerospace applications. Academic Press.

Testa, C., Porcacchia, F., Greco, L., Muscari, R., 2018. Effectiveness of Boundary Element Method Hydrodynamic Data for Propeller Hydroacoustics, A. Yucel Odabasi Colloquium Series 3rd International Meeting-Progress in Propeller Cavitation and Its Consequences: Experimental and Computational Methods for Predictions, pp. 77–85, Istanbul, Turkey.

Tu, J., Yeoh, G.-H., Liu, C., 2018. Computational fluid dynamics: a practical approach. Butterworth-Heinemann.

Versteeg, H., Malalasekera, W., 2007. An Introduction to Computational Fluid Dynamics: The Finite Volume Method, 2nd edition. ed. Prentice-Hall, Harlow, England ; New York.

Wang, X., Walters, K., 2012. Computational analysis of marine-propeller performance using transition-sensitive turbulence modeling. J. Fluids Eng. Trans. ASME 134, 1–10. https://doi.org/10.1115/1.4005729

Wilcox, D.C., 2006. Turbulence Modeling for CFD, 3rd edition, DCW Industries, La Canada, CA.

Zhai, Z.J., Zhang, Z., Zhang, W., Chen, Q.Y., 2007. Evaluation of various turbulence models in predicting airflow and turbulence in enclosed environments by CFD: Part 1 - Summary of Prevalent Turbulence Models. Hvac&R Res. 13, pp. 853–870. https://doi.org/10.1080/10789669.2007.10391460